bioRxiv preprint doi: https://doi.org/10.1101/796722; this version posted March 26, 2020. The copyright holder for this preprint (which was not certified by peer review) is the author/funder, who has granted bioRxiv a license to display the preprint in perpetuity. It is made available under aCC-BY 4.0 International license.

Genome-scale Model Constrained by Proteomics Reveals Metabolic Changes in *Streptomyces coelicolor* M1152 Compared to M145

Snorre Sulheim[1,2], Tjaša Kumelj[2], Dino van Dissel[1], Ali Salehzadeh-Yazdi[3], Chao Du[4], Gilles P. van Wezel[4], Kay Nieselt[5], Eivind Almaas[2,6], Alexander Wentzel[1], Eduard J Kerkhoven[7,8,*]

1. Department of Biotechnology and Nanomedicine, SINTEF Industry, Trondheim, Norway
2. Network Systems Biology Group, Department of Biotechnology and Food Science, NTNU - Norwegian University of Science and Technology, Trondheim, Norway
3. Department of Systems Biology and Bioinformatics, Faculty of Computer Science and Electrical Engineering, University of Rostock, Rostock, Germany
4. Microbial Biotechnology, Institute of Biology, Leiden University, Leiden, The Netherlands
5. Integrative transcriptomics, Center for Bioinformatics, University of Tübingen, Tübingen, Germany

bioRxiv preprint doi: https://doi.org/10.1101/796722; this version posted March 26, 2020. The copyright holder for this preprint (which was not certified by peer review) is the author/funder, who has granted bioRxiv a license to display the preprint in perpetuity. It is made available under aCC-BY 4.0 International license.

6. K.G. Jebsen Center for Genetic Epidemiology, Department of Public Health and General Practice, NTNU - Norwegian University of Science and Technology, Trondheim, Norway
7. Systems and Synthetic Biology, Department of Biology and Biological Engineering, Chalmers University of Technology, Gothenburg, Sweden
8. Novo Nordisk Foundation Center for Biosustainability, Chalmers University of Technology, Gothenburg, Sweden

∗ Corresponding author. Email: eduardk@chalmers.se

Abstract

Many biosynthetic gene clusters (BGCs) in the genomes of environmental microorganisms require heterologous expression in order to realize their genetic potential, including cryptic and metagenomic BGCs. *Streptomyces coelicolor* M1152 is a widely used host strain for the heterologous expression of BGCs, as it has been genetically engineered for this purpose via the deletion of four of its native biosynthetic gene clusters (BGCs) and the introduction of a point mutation in the *rpoB* gene that encodes the beta subunit of RNA polymerase. This latter mutation was shown to have a strong positive impact on antibiotic biosynthesis that remains poorly understood. Therefore, a systemic understanding of the consequences on cellular metabolism of the genomic changes of M1152 could greatly contribute to this understanding. Here we carried out a comparative analysis of M1152 and its ancestor strain M145, connecting observed phenotypic differences to changes in transcript and protein abundance. Measured protein abundance was used to constrain an amended genome-scale model (GEM) and to predict metabolic fluxes. This approach connects observed differences in growth rate and glucose consumption to changes in central carbon metabolism,

bioRxiv preprint doi: https://doi.org/10.1101/796722; this version posted March 26, 2020. The copyright holder for this preprint (which was not certified by peer review) is the author/funder, who has granted bioRxiv a license to display the preprint in perpetuity. It is made available under aCC-BY 4.0 International license.

accompanied by differential expression of important regulons. Our results suggest that precursor availability is not limiting the biosynthesis of secondary metabolites. This implies that alternative strategies could be beneficial for further development of *S. coelicolor* for heterologous production of novel compounds.

Importance

This study provides the first systems description of *S. coelicolor* M1152, an engineered host widely used for the heterologous expression of BGCs directing the synthesis of natural products. By combining time-series proteomics and transcriptomics, batch fermentation data and genome-scale modelling, we can connect observed phenotypes to known genetic modifications and find extensive metabolic rewiring in the M1152 strain compared to the wild-type stain M145. Our study indicates that the deletion of secondary metabolite biosynthetic pathways thought to enhance precursor availability, only has a minor impact on the ability of the modified strain to produced heterologous molecules. In contrast, the *rpoB* mutation is likely responsible for the most dramatic changes in regulatory features and precursor availability. The amended genome-scale model, reconstructed in an open-science framework, allowed us to contextualize the transcriptional changes. This framework facilitates further development by the research community in an organized manner, including version control, continuous integration and quality control and tracking of individual contributions.

Introduction

The bacterium *Streptomyces coelicolor* has been the *de facto* model actinomycete for the production and regulation of antibiotics (1). Being known for over 100 years, the interest in

bioRxiv preprint doi: https://doi.org/10.1101/796722; this version posted March 26, 2020. The copyright holder for this preprint (which was not certified by peer review) is the author/funder, who has granted bioRxiv a license to display the preprint in perpetuity. It is made available under aCC-BY 4.0 International license.

this organism predates the golden age of antibiotic research. With its complex life cycle, featuring mycelial growth and differentiation, spore formation, programmed cell death and the ability to produce multiple secondary metabolites, including calcium-dependent antibiotic (CDA) and the conveniently coloured actinorhodin (Act, blue) and undecylprodigiosin (Red, red), it has assisted greatly in our understanding how streptomycetes sense their surrounding (2–6), activate their developmental cycle (7) and regulate the production of antibiotics (8, 9). Further aided by the publication of its genome sequence (10), the antibiotic coelimycin P1 (yellow), produced from the formerly cryptic polyketide gene cluster known as *cpk*, was added to this list (11). Today, the widespread use of *S. coelicolor* continues as a host for heterologous production of biosynthetic gene clusters (BGCs) (12–17). Heterologous expression is a powerful strategy for novel compound discovery from BGCs that are either natively silent or originate from an unculturable source (18). Both are large untapped resources of microbial biodiversity, nowadays made evident and accessible due to recent advances within the fields of metagenomics, molecular biology and bioinformatics (19).

The efficiency of *S. coelicolor* as a heterologous production host relies on a metabolism that has evolved to provide the necessary precursors to produce a broad range of complex molecules. Many of these molecules are produced when the strain is experiencing nutrient-limiting conditions that lead to growth cessation and complex re-modelling of its metabolism (20). Metabolic switching in *S. coelicolor* M145 in response to phosphate and glutamate depletion has previously been studied in detail at a wide variety of metabolic levels (1–3), unravelling a complex sequence of switching events that ultimately lead to the biosynthesis of the antibiotics CDA, Red and Act. The biosynthesis of coelimycin P1 occurs earlier than the

bioRxiv preprint doi: https://doi.org/10.1101/796722; this version posted March 26, 2020. The copyright holder for this preprint (which was not certified by peer review) is the author/funder, who has granted bioRxiv a license to display the preprint in perpetuity. It is made available under aCC-BY 4.0 International license.

three other compounds in the growth cycle and appears to be independent of the major metabolic switch (8).

To improve *S. coelicolor* M145 as a host for heterologous BGCs expression, strain M1146 was created by the sequential deletion of its four major BGCs (*act, red, cda* and *cpk*) (13). This should increase precursor availability for the production of a whole range of heterologous products and provides a cleaner chromatographic background to easier identify novel compounds. *S. coelicolor* M1152 is a derivative of M1146, that besides the deletion of the four main BGCs bears the C1298T point mutation in the *rpoB* gene that encodes the beta subunit of RNA polymerase. This mutation was shown to have strong positive effects on the production of various antibiotics (13, 22). Up to now, M1152 is a preferred general 'superhost' for heterologous BGC expression (12, 16, 23–25) and is the starting point for further strain development.

A hurdle in further development of *S. coelicolor* as a 'superhost' is the limited knowledge of M1152 metabolism and its regulatory systems, even if some insight can be gained from analysing snapshots of gene expression levels during regular time intervals of a batch fermentation (26–30). Since enzymes are catalysing most metabolic transformations, assessing protein abundance or gene expression contributes to the elucidation of metabolic behaviour. Here, we therefore apply proteomics data as constraints (31) on a genome-scale metabolic model (GEM) of *S. coelicolor* to reveal how proteome changes affect the metabolic fluxes during the different stages of growth and development, and how the metabolism of *S. coelicolor* M1152 differs from its parent strain, M145.

GEMs are both valuable resources of strain-specific knowledge, mathematical models able to predict steady-state flux distributions, and frameworks for interpretation and integration of

bioRxiv preprint doi: https://doi.org/10.1101/796722; this version posted March 26, 2020. The copyright holder for this preprint (which was not certified by peer review) is the author/funder, who has granted bioRxiv a license to display the preprint in perpetuity. It is made available under aCC-BY 4.0 International license.

different 'omics' data, e.g. transcriptomics and proteomics (32). The increased interest in using genome-scale models of *S. coelicolor* is conspicuous. Since the first reconstruction in 2005 (33), five GEMs have been published (15, 34–37), including three in 2018: iKS1317 (15), Sco4 (37) and iAA1259 (35). Additionally, as a model organism for the *Actinomycetes,* the GEMs of *S. coelicolor* are frequently used as template for model development of closely related strains (38), such as *S. clavuligerus* (39), *Saccharopolyspora erythraea* (40) and *S. lividans* (41). The recent updates of the *S. coelicolor* GEM were developed in parallel by different research groups: while all groups share the common interest of utilizing a high-quality model for predictions and data analysis, the prevailing approach of independent parallel development is inefficient. Additional to duplicating a considerable amount of work, lack of common standards for documentation of progress and issues, evaluation of model performance, as well as the use of different annotations makes it cumbersome to compare and merge models.

To increase the rate and quality of model reconstruction, in this study two research groups of the Sco-GEM community, responsible for two of the latest model updates (15, 37), have joined forces to merge existing GEMs of *S. coelicolor* into one consensus-model that is publicly hosted on GitHub and can be continuously updated and improved by all members of the community. Hosting the model on GitHub has many advantages: (i) open access and contribution; (ii) version control; (iii) continuous development and integrated quality control with memote (42); (iv) new improvements released instantly (no publication lag time); and (v) complete documentation of model reconstruction. Such an approach has historic precedents: model reconstruction as a community effort has been a success for the human GEM (43), baker's yeast (44–49) and Chinese Hamster Ovary cells (50). The recent developments in *S. coelicolor* model and strain improvements in different research groups

bioRxiv preprint doi: https://doi.org/10.1101/796722; this version posted March 26, 2020. The copyright holder for this preprint (which was not certified by peer review) is the author/funder, who has granted bioRxiv a license to display the preprint in perpetuity. It is made available under aCC-BY 4.0 International license.

prove that it is an opportune time now to join forces in the *Streptomyces* modelling efforts as well.

Results

Improvement of Sco-GEM

We conducted a stepwise reconstruction of Sco-GEM, the consensus genome-scale metabolic model of *S. coelicolor*, while tracking development using Git for version control (**Figure 1A; Data Set S1, Tab 1**). Sco-GEM is the most comprehensive and highest quality GEM of this organism (**Figure 1B**), comprising 1777 genes, 2612 reactions, 2073 metabolites and a memote score of 77%, which is indicative of the overall model quality (42). Sco-GEM features an accuracy of 96.5% and 74.5% (**Figure 1C**) in predicting correct phenotypes for growth environments and knockout mutants, respectively, yielding in total a Matthews Coefficient of Correlation of 0.53 with the test data previously described (15).

Sco-GEM has been reconstructed by curating the recently published iKS1317 model (15) to include genes, reactions and metabolites from the equally recently published models iAA1259 (35) and Sco4 (37). While the curations from iAA1259 were primarily related to coelimycin P1, butyrolactone, xylan and cellulose pathways, the 377 reactions added to Sco-GEM from Sco4 were scattered across a large range of different subsystems, covering both primary and secondary metabolism (**Figure S1**).

Subsequent to merging the existing *S. coelicolor* GEMs, we performed a number of further curations of the model: including improvement of annotations, both in terms of coverage and number of different databases, e.g. KEGG (51, 52), BioCyC (53), ChEBI (54) and MetaNetX (55). All reactions and metabolites have been given identifiers according to the

bioRxiv preprint doi: https://doi.org/10.1101/796722; this version posted March 26, 2020. The copyright holder for this preprint (which was not certified by peer review) is the author/funder, who has granted bioRxiv a license to display the preprint in perpetuity. It is made available under aCC-BY 4.0 International license.

BiGG namespace (56), and all reactions are categorized into 15 different subsystems, covering 128 different pathways.

The biomass composition was curated to reflect estimated levels of prosthetic groups that are associated to cellular proteins. Proteomics data, as discussed below, were used to estimate protein levels, while UniProt (57) provided annotations of proteins with prosthetic groups, which was used to estimate overall prosthetic group levels (**Data Set S1, Tab 2**).

Reaction reversibility updated for almost a third of queried reactions

The determination of reaction directionality and reversibility is an important step in a GEM reconstruction (58). However, the thermodynamic consistency of reactions was not considered in previous *S. coelicolor* models. We calculated Gibbs free energy changes for 770 of the 2612 model reactions (**Data Set S1, Tab 3**) using eQuilibrator (59), and inconsistencies in assigned reaction bounds transpired from a significant overlap of the range of Gibbs free energies between reversible and irreversible reactions (**Figure 1D**). A relatively lenient threshold of −30 kJ/mol was defined to classify a reaction as irreversible; with the intent not to over-constrain the model (**Figure 1E**). The proposed changes in reversibility were evaluated against growth and knockout data (15), discarding 59 of 770 of the proposed reactions. Consequentially, the flux bounds of 273 reactions were modified, while all ATP-driven reactions were manually curated and generally assumed irreversible, unless they had an estimated positive change in Gibbs free energy or were known to be reversible. Examples of this include nucleoside diphosphate kinase (60) and ATP synthase (61).

Curation of transport reactions

As transport reactions have previously not been extensively curated in *S. coelicolor* models, we performed a thorough curation of transporters by querying various databases and BLAST

bioRxiv preprint doi: https://doi.org/10.1101/796722; this version posted March 26, 2020. The copyright holder for this preprint (which was not certified by peer review) is the author/funder, who has granted bioRxiv a license to display the preprint in perpetuity. It is made available under aCC-BY 4.0 International license.

analysis as detailed in Materials and Methods. This culminated in adding 43 new transport reactions and updating 39 of the 262 existing reactions in Sco-GEM (**Figure 1F; Data Set S1, Tab 4**). The majority of the transporters comprises primary active transport proteins and secondary carriers (46%), in accordance with previous work (62). Most primary active transporters are ATP-binding cassette (ABC) transporters (30%), while proton symports (30%) dominate the secondary carriers.

Development of the enzyme-constrained model EcSco-GEM

To include explicit constraints regarding enzymes catalysing metabolic reactions, the GECKO formalism (31) was applied to introduce enzyme turnover rates (k_{cat}) and prepare the model for integration of proteome data. Note that this approach regards the maximum catalytic activities but does not consider other kinetic parameters such as affinity constants. The flux variability of the resulting enzyme-constrained model (EcSco-GEM) is strongly reduced compared to the classic genome-scale model (**Figure 1G**), as infeasible solutions due to limitation in protein allocation are discarded, significantly improving model predictions. From this, 17 time- and strain-specific EcSco-GEM models were generated by incorporation of estimated growth-, secretion- and uptake rates, as well as proteome data from cultivations that are detailed and analysed below.

Framework for further development of Sco-GEM by the community

The Sco-GEM model is hosted as an open repository as suggested by memote, a recently developed tool for transparent and collaborative model development (42). The memote tool is incorporated in the repository through Travis CI and tracks the model development on every change of the model. Sco-GEM v1.2.0 achieved a memote-score of 77%, which is superior to any previous model of *S. coelicolor* (**Figure 1B; Supplemental Information**).

bioRxiv preprint doi: https://doi.org/10.1101/796722; this version posted March 26, 2020. The copyright holder for this preprint (which was not certified by peer review) is the author/funder, who has granted bioRxiv a license to display the preprint in perpetuity. It is made available under aCC-BY 4.0 International license.

Hosting Sco-GEM on GitHub with memote integration ensures continuous quality control and enables public insight into all aspects of model reconstruction and curation: any user can report errors or suggest changes through issues and pull requests. As contributions to the model development are fully trackable and can therefore be credited fairly, Sco-GEM is positioned as a community model that we envision to be continuously updated and widely used by the *S. coelicolor* research community.

In the remaining parts of the Results section, we have applied Sco-GEM along with transcriptome and proteome data, to study and compare the responses of *S. coelicolor* M145 and M1152 to phosphate depletion on a systems level and for the first time provide detailed insight into the distinct physiological features of engineered 'superhost' strain M1152, which will be of value for its further development.

The enzyme-constrained model connects regulatory changes in *S. coelicolor* M145 in response to phosphate depletion with the production of the major secondary metabolites.

To evaluate whether the (Ec)Sco-GEM models can simulate behaviours of *S. coelicolor* metabolism, we performed and analysed time-course sampled cultivations of secondary metabolite producing strain M145 in the context of the generated models. For that purpose, *S. coelicolor* M145 was cultivated in batch fermentations using standardized protocols reported earlier (20). Cultures were sampled for 'omics data, as well as substrate utilization and secondary metabolite measurements to identify regulatory, proteomic and metabolic changes during the metabolic switch. The online and offline measurements showed that phosphate depletion in the cultivation medium was reached approximately 35 hours after

bioRxiv preprint doi: https://doi.org/10.1101/796722; this version posted March 26, 2020. The copyright holder for this preprint (which was not certified by peer review) is the author/funder, who has granted bioRxiv a license to display the preprint in perpetuity. It is made available under aCC-BY 4.0 International license.

inoculation. Shortly after, the culture growth ceased, and first Red and subsequently Act were detected in the culture medium (**Figure 2A and 2B)**. Both D-glucose and L-glutamate were consumed concomitantly, and their consumption continued after phosphate depletion, while both remained in excess until the end of cultivation. Note that *Streptomyces* can utilize intracellular phosphate storages after the medium is phosphate depleted (63). The RNA-seq and untargeted proteomic data were analysed in the light of previous studies (8, 9) and were in good agreement with data previously obtained from microarrays or targeted proteomics (8, 34) (**Figure 2C and S2**). This confirmed the high reproducibility of the experiments across independent cultivations and high reliability of the chosen cultivation and analytic procedures (**Figure 2**).

The proteome data were incorporated into EcSco-GEM to yield time-specific metabolic models of M145, giving insight on the changes occurring in the metabolic activity of different pathways during batch cultivation. Metabolic fluxes were estimated using an unbiased approach of random sampling, as alternative to optimization of a well-defined cellular objective used in flux balance analysis (64). It is possible that *S. coelicolor* is wired to maximize its growth rate prior to phosphate depletion, but after the metabolic switch, it is difficult to define a clear cellular objective. We applied an approach that samples the vertices of the solution space (65), and used their mean values to compare the metabolic fluxes between the two strains and between different time points. The general overview from **Figure 2D** is an initial validation of the model. It shows that the metabolic switch induces a large shift in global gene expression (8) and predicts that the most drastic changes in fluxes occur in response to phosphate depletion.

bioRxiv preprint doi: https://doi.org/10.1101/796722; this version posted March 26, 2020. The copyright holder for this preprint (which was not certified by peer review) is the author/funder, who has granted bioRxiv a license to display the preprint in perpetuity. It is made available under aCC-BY 4.0 International license.

The response to phosphate depletion from the medium is achieved by a set of genes, positively regulated by PhoP, that are involved in phosphate scavenging, uptake and saving (66–68). The metabolic switch can be readily identified by the rapid upregulation of this regulon after 35 hours of cultivation in M145 and 47 hours in M1152 (**Figure 2C**). PhoP also negatively regulates nitrogen assimilation (69), which can partly explain the change in amino acids metabolism after phosphate depletion. Indeed, from the RNA-seq data we find that glutamate import, the glutamate sensing system *gluR-gluK* (70), *glnR* (71) and *glnA* are downregulated immediately subsequent to phosphate depletion (**Figure S3**). Since PhoP is also known to regulate negatively the biosynthesis of secondary metabolites, the switching of its expression likely delays these pathways (69, 72). However, after 37 hours of cultivation the upregulation of the *cda* and *red* genes was observed, whereas that of the *act* genes was initiated at 41 hours (**Figure 2E**). Production of Red and Act was measurable in the culture medium after 41 and 49 hours of cultivation, respectively (**Figure 2B**). The enzyme-constrained models predict an immediate increase in fluxes through the biosynthetic pathways for the four main compounds Act, Red, CDA and coelimycin P1 after the metabolic switch (**Figure 2D**).

The onset of secondary metabolism is strongly correlated with an increase in oxidative phosphorylation and a decrease in fatty acid biosynthesis in M145.

The metabolic switch was shown to be correlated with an enhanced degradation of branched-chain amino acids (valine, leucine and isoleucine), an increase in oxidative phosphorylation and a decrease in fatty acid biosynthesis (**Figure 2D and S4**). An active oxidative phosphorylation relies on an active TCA cycle that generates reduced co-factors whose re-oxidation by the respiratory chain generates a proton gradient that drives ATP synthesis by the ATP synthase. The feeding of the TCA cycle requires acetyl-CoA, as well as

bioRxiv preprint doi: https://doi.org/10.1101/796722; this version posted March 26, 2020. The copyright holder for this preprint (which was not certified by peer review) is the author/funder, who has granted bioRxiv a license to display the preprint in perpetuity. It is made available under aCC-BY 4.0 International license.

nitrogen. Nitrogen likely originates from degradation of glutamate and branched-chain amino acids, whereas acetyl-CoA likely originates from glycolysis, as well as from the degradation of these amino acids as previously demonstrated (73). Indeed, the model predicts an increased flux through citrate synthase feeding acetyl-CoA into the TCA cycle (**Figure S5A).** The predicted increase in oxidative phosphorylation is supported by the RNA-seq data showing upregulation of enzymes belonging to the respiratory chain (**Figure S5B**). This is consistent with the clear correlation previously reported between high ATP/ADP ratio, resulting from an active oxidative phosphorylation, and actinorhodin production (74). Furthermore, the consumption of acetyl-CoA by the TCA cycle to support the oxidative metabolism logically impairs fatty acids biosynthesis (74).

The pentose phosphate pathway provides the main redox cofactor NADPH for polyketide biosynthesis, as well as to combat oxidative stress, and its model-predicted flux increase upon initiation of polyketide synthesis is in agreement with previous studies (75, 76). A clear positive correlation was also noticed between the biosynthesis of alanine, aspartate and glutamate, which are precursors for CDA and/or coelimycin P1 (**Figure 2D**) and the biosynthesis of these antibiotics. Similar observations were made in the antibiotic-producing *Amycolatopsis sp.* (77). Our EcSco-GEM model proved to be in good agreement with previously reported findings, indicating that it is able to capture *S. coelicolor* metabolic behaviour.

bioRxiv preprint doi: https://doi.org/10.1101/796722; this version posted March 26, 2020. The copyright holder for this preprint (which was not certified by peer review) is the author/funder, who has granted bioRxiv a license to display the preprint in perpetuity. It is made available under aCC-BY 4.0 International license.

Model-assisted characterization of engineered *S. coelicolor* M1152 and its responses to phosphate depletion.

As detailed above, EcSco-GEM shed a new light on the metabolic switch in secondary metabolite producing strain M145. *S. coelicolor* M1152 (13) is a M145 derivative devoid of the four major BGCs and bearing a point mutation in the *rpoB* gene. A better systemic understanding of M1152 metabolism would benefit to its further development as a performing host. To do so, a comparative analysis of gene expression levels and metabolic fluxes was carried out in the strains M145 and M1152.

Batch cultivations of M1152 were performed using identical conditions and comparable sampling regimes as for M145 reported above. This enabled a direct comparison of the two strains at a systems level, revealing both expected and unexpected effects of the strains' genetic differences (**Figure 3**). As anticipated, the products of the Cpk, CDA, Red, and Act biosynthetic pathways were undetectable in M1152 (**Figure 3A**). As previously observed (13), the growth rate of M1152 is reduced compared to M145 (0.15 h^{-1} vs 0.21 h^{-1} in the initial exponential growth phase), delaying phosphate depletion by M1152 to 47 hours after inoculation (**Figure 3A**).

The sampling time points for proteome and transcriptome were adjusted accordingly (**Figure 3B**), enabling pairwise comparison of measurements between the two strains. Genes responsive to phosphate depletion, members of the PhoP regulon (8), were used to align the different sample datasets for M145 or M1152 (**Figure 3C**). Interestingly, most of the responses of M145 to phosphate depletion were retained in M1152 (**Figure 3D**). Principle component analysis of the proteome data confirms high consistency between corresponding biological replicates and incremental changes between sample points for both M145 and

bioRxiv preprint doi: https://doi.org/10.1101/796722; this version posted March 26, 2020. The copyright holder for this preprint (which was not certified by peer review) is the author/funder, who has granted bioRxiv a license to display the preprint in perpetuity. It is made available under aCC-BY 4.0 International license.

M1152 (mainly explained by PC1: 18.6% variance, **Figure 3E**). A clear strain dependent clustering of the data (PC2: 15.5% variance) indicates global significant differences at the protein level. EcSco-GEM was subsequently used to predict metabolic changes in M1152 (**Figure 3E**).

The different glutamate and glucose consumption rates of M145 and M1152 (**Figure 4A and 4B**) resulted in substantial metabolic differences between the two strains prior to phosphate depletion. During cultivation on SSBM-P medium, where glutamate is the sole nitrogen source, glucose and glutamate are co-consumed. M1152, as M1146 (74), has a reduced specific glucose uptake rate compared to M145. It thus obtains a larger share of its carbon from glutamate (**Figure 4A and 4B**) and has consequently also a higher nitrogen availability than M145. A reduced flux through glycolysis has also been reported previously for strain M1146 (78). This might be an effect of the predicted increased concentration of ATP in M1146 compared to M145, which inhibits glucose uptake and phosphofructokinase (74, 78). Since Act was proposed to act as an electron acceptor reducing the efficiency of the oxidative phosphorylation, it is suggested that the lack of Act in M1146 causes the elevated ATP levels (74). However, we find the largest difference in glycolytic flux at early time points, prior to phosphate depletion and Act production in M145, proving that Act itself cannot explain this observation.

The EcSco-GEM predicts the consequences of the reduced glucose uptake of M1152 on its central carbon metabolism (**Figure 4C**). A less active glycolysis in M1152 than in M145 leads to a lower carbon flow towards acetyl-CoA and thus lower excretion of acetate compared to M145 (**Figure 4B**). Furthermore, EcSco-GEM reveals an increased flux from glutamate to alpha-ketoglutarate. Indeed, a fraction of the pool of oxaloacetate might be converted into

bioRxiv preprint doi: https://doi.org/10.1101/796722; this version posted March 26, 2020. The copyright holder for this preprint (which was not certified by peer review) is the author/funder, who has granted bioRxiv a license to display the preprint in perpetuity. It is made available under aCC-BY 4.0 International license.

alpha-ketoglutarate by aspartate transaminase to feed the TCA cycle. The rest might be converted into phosphoenolpyruvate (PEP) by PEP carboxykinase for gluconeogenesis, since PEP carboxykinase was shown to carry higher fluxes in M1152 than in M145 (**Figure 4C**).

Since recent studies have demonstrated a reverse correlation between antibiotic and triacylglycerol biosynthesis in *S. lividans* and *S. coelicolor* (74, 79), one can speculate that the acetyl-CoA/malonyl-CoA units yielded by glycolysis for the biosynthesis of antibiotics in M145 are being used for enhanced growth and/or fatty acids and TAG biosynthesis in M1152. However, this is likely not the case, as M1152 has rather a reduced growth rate compared to M145, and fatty acid biosynthesis remains downregulated after the switch (**Figure 5**). It is noteworthy that the flux toward this acetyl-CoA/malonyl-CoA sink is still 3- to 6-fold larger than the total flux going into secondary metabolite biosynthesis. We thus propose that together with enhanced nitrogen availability, acetyl-CoA made available from the deletion of these BGCs is used to feed the TCA cycle to support the oxidative metabolism in M1152. This would generate oxidative stress whose toxic effects might be responsible for the growth delay of this strain.

Transcriptome analysis reveal differential expression of global regulators

While the proteome data are an integral part of the EcSco-GEM models, RNA-seq data were used to both verify the trends and to gain further insights in the regulatory changes that are not captured by the metabolic models. As the proteomic data, the RNA-seq data showed large global differences between M1152 and M145, revealing 499 differentially expressed genes with a significance threshold of $p<0.01$.

Unsupervised clustering of the significantly changed genes reveal differences in regulatory systems related to redox regulation, signalling and secondary metabolism. The significantly

bioRxiv preprint doi: https://doi.org/10.1101/796722; this version posted March 26, 2020. The copyright holder for this preprint (which was not certified by peer review) is the author/funder, who has granted bioRxiv a license to display the preprint in perpetuity. It is made available under aCC-BY 4.0 International license.

359 changed genes were clustered into 7 groups with K-means clustering, with clusters 1-3
360 containing genes that are upregulated in M1152 compared to M145 and clusters 4-7 vice
361 versa (**Figure S6A and Data Set S1, Tab 5**). A Gene Ontology (80, 81) enrichment analysis of
362 the seven clusters was conducted to identify upregulated processes in each of the two
363 strains (**Figure S7**, **cf. Figure S6A**).

364 The enriched processes upregulated in M1152 point to increased oxidative stress (**Figure S7**):
365 antioxidant and peroxidase activity (SCO2633 [sodF]; SCO4834-35) in addition to
366 biosynthesis of carotenoid (SCO0185–SCO0188), a known antioxidant (82, 83). The putative
367 proteins within the cytochrome-P450 family (SCO7416–SCO7422) found in cluster 1 might
368 also be linked to increased oxidative stress (84), but also to oxidation of precursors used for
369 the synthesis of macrolides (85). Indeed, by comparing the time series expression levels for
370 genes related to oxidative stress we observe that the majority of genes related to oxidative
371 stress are upregulated in M1152 (**Figure 6**). These changes correlate to a more active
372 oxidative metabolism and TCA cycle as predicted by Ec-ScoGEM (**Figure 4**).

373 In cluster 2 we find *scbA* (SCO6266) and its downstream gene *scbC* (SCO6267), which stands
374 out by being almost 6-fold upregulated in M1152. This high expression level is likely due to
375 the deletion of *scbR2* (SCO6286), the last gene selected to be part of the *cpk* BGC (86).
376 Besides regulation of the *cpk* cluster, ScbR2 binds upstream of several global regulators of
377 development and secondary metabolism, including AfsK, SigR, NagE2, AtrA, AdpA and ArgR
378 (87). It also acts together with ScbR to regulate ScbA, which produces the y-butyrolactone
379 SCB1. However, when looking at the genes regulated by ScbR (87), we only observe a clear
380 difference in expression for genes regulated by AfsR (phosphorylated by AfsK) (88, 89), while
381 this is not the case for genes regulated by ArgR, AdpA or ScbR itself (**Figure S5C-F**).

bioRxiv preprint doi: https://doi.org/10.1101/796722; this version posted March 26, 2020. The copyright holder for this preprint (which was not certified by peer review) is the author/funder, who has granted bioRxiv a license to display the preprint in perpetuity. It is made available under aCC-BY 4.0 International license.

Amongst the genes upregulated in M145, in cluster 4 we find genes related to the redox regulated transcription factor SoxR (90), and a similar pattern is observed for the entire SoxR regulon (**Figure S6B**). SoxR is known to react directly to the presence of actinorhodin (91, 92), and indeed, in M145 this group of genes follows the production profile of actinorhodin, while their expression remains low in M1152 since Act is not produced. The benzoquinone Act, as electron acceptor, is thought to reduce respiration efficiency and thus energy charge as well as to combat oxidative stress (74). Consistently, the RNA-seq data revealed that the ATP-synthase gene cluster (SCO5366–SCO5374) was upregulated almost 2-fold in M1152 compared to M145, most prominently in the stationary phase during Act production (**Figure S6C**). This agrees with observations in the M1146 strain (78). Cluster 4 also contains the genes directly up- and downstream of the deleted actinorhodin BGC in M1152 (SCO5071–SCO5072, encoding 3-hydroxyacyl-CoA dehydrogenase, and SCO5091–SCO5092, encoding a two-component flavin-dependent monooxygenase system) (93). In clusters 5, 6 and 7 we find genes with reduced expression in M1152, and the enriched processes are related to cellular and iron ion homeostasis, development, signalling and morphology. This corresponds to the delayed sporulation observed for M1152 (13).

Elevated expression of ribosomal proteins in M1152 after phosphate depletion

An increased transcription of genes encoding ribosomal proteins could be observed in M1152 after phosphate depletion (**Figure S6D**). The *rpoB* mutation of the RNA polymerase present in M1152 is thought to induce a conformational change mimicking the binding of guanosine tetraphosphate (ppGpp) to this enzyme (22). ppGpp is synthesized in response to nutritional stress and reduces the transcription of genes related to active growth, such as genes encoding ribosomal RNAs and ribosomal proteins (94), whereas it up-regulates those

bioRxiv preprint doi: https://doi.org/10.1101/796722; this version posted March 26, 2020. The copyright holder for this preprint (which was not certified by peer review) is the author/funder, who has granted bioRxiv a license to display the preprint in perpetuity. It is made available under aCC-BY 4.0 International license.

involved in development/differentiation and antibiotic production (95, 96). In consequence the up-regulation of ribosomal proteins was unexpected in M1152, especially since the expression of the ppGpp regulon was not found to be significantly changed in M1152 (**Figure S5G and S5H**). However, since high nucleoside triphosphate levels are known to have a positive impact on ribosome synthesis (97), we hypothesize that the higher ATP content of M1152 compared to M145, after phosphate depletion, may be responsible for the differences in expression of ribosomal proteins. Such difference in ribosomal protein expression is mainly seen in the antibiotic production phase and correlated with production of Act in M145, which has a negative impact on the energetic state of the cell (74).

Reduced production of the polyketide germicidin in M1152

It is usually thought that removal of sinks consuming valuable precursors improves the ability of a strain to produce heterologous metabolites requiring these precursors for their biosynthesis. It was therefore unexpected that the production rate (in ng ml^{-1} $hour^{-1}$) of the polyketides germicidin A and B (98), autologous to both M145 and M1152, was reduced by 92% and 82% for germicidin A and B in M1152, respectively (**Figure 7**). This could be explained by the more active oxidative metabolism of M1152 compared to M145. In M1152 the pool of acetyl-CoA would thus be used to feed the TCA cycle rather than be used for germicidin biosynthesis.

To further understand the cause of the reduced production in M1152, we also measured the production of germicidin in the intermediate strain M1146 (**Figure 7, Figure S6E**), which does not feature the *rpoB* mutation but is missing the 4 BGCs also deleted in M1152 (13). The production rate of germicidin A and B in M1146 was found to be reduced by 27% and 25%, respectively, compared to M145. This demonstrates that, while the removal of BGCs may

bioRxiv preprint doi: https://doi.org/10.1101/796722; this version posted March 26, 2020. The copyright holder for this preprint (which was not certified by peer review) is the author/funder, who has granted bioRxiv a license to display the preprint in perpetuity. It is made available under aCC-BY 4.0 International license.

influence polyketide production, a strong reduction appears to be assignable to the *rpoB* mutation in M1152.

Discussion

In this work, we carried out a multi-omics study to compare the metabolic changes of *Streptomyces coelicolor* M145 and the BGC-deletion mutant M1152 during batch fermentation. The defined cultivation medium used in this work was chosen because it supports sufficient growth and a delayed, well-defined onset of secondary metabolism, necessary to study the metabolic switch (20). We aimed at defining the metabolic features differing between the two strains, both during exponential growth and stationary phase after phosphate depletion.

To achieve this from a systems biology perspective, we combined time-course sampled cultivation and transcriptome analysis with enzyme-constrained genome-scale models generated with proteome data. Such genome-scale models are extensively used to connect transcriptome- and proteome data to metabolic fluxes. Leveraging metabolic simulations to contextualize transcriptional changes is mainly impacted by the quality of the computational model used. Here, two teams joined efforts to improve a consensus model of *S. coelicolor*, yielding a comprehensive model useful for the scientific community.

Genome-scale models provide hypothesis for slow growth of M1152

The reduced growth rate of M1152 is correlated with reduced glucose uptake and enhanced glutamate uptake compared to M145. This is expected to lead to a less active glycolysis but a more active TCA cycle, and thus, a more active oxidative metabolism in M1152 compared to M145. An active oxidative metabolism is known to generate oxidative stress, and indeed, the *in vivo* data, as well as the genome-scale model, predict an increased oxidative stress in

bioRxiv preprint doi: https://doi.org/10.1101/796722; this version posted March 26, 2020. The copyright holder for this preprint (which was not certified by peer review) is the author/funder, who has granted bioRxiv a license to display the preprint in perpetuity. It is made available under aCC-BY 4.0 International license.

M1152. The toxicity of oxidative stress might, at least in part, be responsible for the growth delay of M1152, while the *rpoB* mutation may add to this phenotype, since one of the functions of the ppGpp-associated RNA polymerase is to promote a growth arrest in conditions of nutritional stress.

Further development may improve M1152 as host for heterologous expression

The strain M1152 has several advantages as a host for heterologous production of secondary metabolites. The deletion of the 4 major BGCs not only removes presumed competing sinks for valuable precursors, but also generates a clean background to ease the identification of novel products by mass spectrometry. M1152 was already proven to be more efficient than M145 and M1146 in heterologous production of the nitrogen-containing antibiotics chloramphenicol and congocidine, as well as Act production from reintroduction of its BGC (13). Strains M1146 and M1152 produce, respectively, 3- to 5-, and 20- to 40-fold more chloramphenicol and congocidine from respective heterologous clusters than M145. Furthermore, in strain M1317, derived from M1152 by additional removal of three Type III PKS genes (16), the (re-)introduction of germicidin synthase gave a 10.7 and 7.8-fold increase in the total germicidin production by M1317 and M1152, respectively. This demonstrated that the *rpoB* mutation, earlier shown to have a positive impact on the biosynthesis of secondary metabolites (13), has a higher impact on the production of these compounds than the deletion of competing precursor sinks, even while it cannot be excluded that unintended and unknown genetic differences introduced during strain development are underlying some of the observed behaviours. Nonetheless, the comparative analysis of M145 and M1152 provides valuable insight to the impact of the *rpoB* mutation on cellular metabolism and its relationships with antibiotic production, while a dedicated, systematic

bioRxiv preprint doi: https://doi.org/10.1101/796722; this version posted March 26, 2020. The copyright holder for this preprint (which was not certified by peer review) is the author/funder, who has granted bioRxiv a license to display the preprint in perpetuity. It is made available under aCC-BY 4.0 International license.

comparative analysis of M1152, M1146 (13) and M145 will be necessary to in detail dissect the overlapping influences of BGC deletion and the *rpoB* mutation (99).

As earlier work has suggested a competition for common precursors (acetyl-CoA/malonyl-CoA) between fatty acids and secondary metabolites biosynthesis (100), it could be anticipated that the deletion of BGCs would have a positive effect on fatty acids, and thus TAG biosynthesis, but our data indicate that this is not the case (**Figure 5**).

Materials and Methods

Sco-GEM consensus model reconstruction and development

A brief description of the model reconstruction process is given in the following section, while all details are described in the **Supplemental Information.** and in the community model's GitHub repository (https://github.com/SysBioChalmers/sco-GEM). The model is hosted on GitHub to facilitate further development by the community, and we've also created a channel on Gitter dedicated to Sco-GEM questions and discussions (https://gitter.im/SysBioChalmers/Sco-GEM).

Protocol for model merging

Using iKS1317 (15) as a starting point, additional reactions, metabolites and genes were added from Sco4 (37) and iAA1259 (35). These three models are all based on the preceding model iMK1208. To facilitate model comparison, modified or added reactions and metabolites in Sco4 and iAA1259 were mapped to the iKS1317 namespace by using reaction and metabolite database annotations, reaction equations and metabolite names and

bioRxiv preprint doi: https://doi.org/10.1101/796722; this version posted March 26, 2020. The copyright holder for this preprint (which was not certified by peer review) is the author/funder, who has granted bioRxiv a license to display the preprint in perpetuity. It is made available under aCC-BY 4.0 International license.

formulas. The full list of reactions and metabolites added or modified according to Sco4 and iAA1259 is given in **Data Set S1, Tab 6 - 10.**

The next step of the reconstruction process involved mainly manual curations: known flaws and missing gene annotations in iKS1317 and Sco4 were fixed; reactions and metabolites added from Sco4 were given IDs according to the BiGG namespace (56); all reactions, metabolites and genes were given SBO annotations (101) (**Data Set S1, Tab 11**); all possible reactions and metabolites were given MetaNetX (55) and chebi (54) (metabolites only) annotations; the extensive annotation of genes from iAA1259 were expanded to cover 1591 of the 1777 genes in Sco-GEM. We also created pseudo-metabolites for the redox cofactors NADH/NADPH and NAD+/NADP+ and introduced them into reactions where the cofactor usage is uncertain.

The biomass equation was curated with the following main improvements: 1) Adopting the curation of 2-demethylmenaquinol and menaquinol from iAA1259; 2) Separating the biomass reaction into the pseudometabolites lipid, protein, dna, rna, carbohydrate, cell wall and misc; 3) Updating the coefficients for prosthetic groups based on the proteomics data and information about prosthetic groups for individual proteins from UniProt. Additional details are given in the **Supplemental Information**.

Model reversibility

By using python-API (https://gitlab.com/elad.noor/equilibrator-api) of eQuilibrator (59) we calculated the change in Gibbs free energy for 770 reactions (**Data Set S1, Tab 3**). eQuilibrator can only calculate the change in Gibbs free energy for intracellular reactions (i.e. not transport and exchange reactions) where all metabolites are mapped to KEGG (51, 52). The calculations are based on the component contribution method (102). The change in

bioRxiv preprint doi: https://doi.org/10.1101/796722; this version posted March 26, 2020. The copyright holder for this preprint (which was not certified by peer review) is the author/funder, who has granted bioRxiv a license to display the preprint in perpetuity. It is made available under aCC-BY 4.0 International license.

Gibbs free energy was calculated at standard conditions (25 °C, 1 bar), pH7 and 1mM concentration of reactants, denoted $\Delta_r G'^{m}$ in eQuilibrator. We then applied a threshold of -30 kJ/mol to define a reaction as irreversible (103, 104). Using the set of growth data and knockout data, we evaluated the effect of these changes in reaction reversibility: by randomly applying these changes to 10 reactions at the time, we identified single, pair and triplets of reactions that reduced model accuracy when the reversibility was changed based on the change in Gibbs free energy (**Data Set S1, Tab 12; Supplemental Information**). Energetic cofactors, including ATP, NADPH, NADH, FAD and any quinone, were involved in 284 of the 770 reactions for which the change in Gibbs free energy was calculated. Of the 114 reactions involving ATP, 82 reactions had an estimated change in Gibbs free energy between ±30 kJ/mol, indicating that the reactions were reversible. Because one assumes that ATP-driven reactions in general are irreversible (58), the reversibility of these 82 reactions were manually curated (**Data Set S1, Tab 13**). For the 7 quinone-associated reactions for which the change in Gibbs free energy was calculated (CYTBD2, NADH17b, NADH10b, MBCOA2, G3PD5, PDH3, NADH2r) all were defined as irreversible as previously suggested (58). The reversibility of reactions involving any of the other energetic cofactors were treated as any other reaction as previously described.

Analysis and annotation of transport reactions

Gene annotations, substrate and transport class information were mostly extracted from Transport DB 2.0 (105) and TCDB (106). Then, transport proteins were extracted from IUBMB-approved Transporter Classification (TC) System and categorized into 9 main classes (**Figure 1F**): 1) ABC transporter; 2) PTS transporter; 3) Proton symporter; 4) Sodium symporter; 5) Other symporter; 6) Proton antiport; 7) Other antiport; 8) Facilitated diffusion; 9) Simple diffusion. For those transport proteins with an ambiguous substrate annotation in

bioRxiv preprint doi: https://doi.org/10.1101/796722; this version posted March 26, 2020. The copyright holder for this preprint (which was not certified by peer review) is the author/funder, who has granted bioRxiv a license to display the preprint in perpetuity. It is made available under aCC-BY 4.0 International license.

TCDB, the specific substrate annotation was obtain by extracting annotations from KEGG (51, 52), UniProt (57) or through BLAST homology search (107) using a similarity threshold of 90% (**Supplemental Information; Data Set S1, Tab 4**).

Development of enzymatically constrained (EcSco-GEM) model

An enzyme-constrained version of the Sco-GEM model (denoted EcSco-GEM) was generated using GECKO (31). The GECKO method enhances an existing GEM by explicitly constraining the maximum flux through each reaction by the maximum capacity of the corresponding enzyme, given by the product of the enzyme abundance and catalytic coefficient. This is facilitated by splitting both, reactions catalysed by isoenzymes and reversible reactions. The Sco-GEM v1.1 model was modified using GECKO version 1.3.4. Kinetic data, in the form of k_{cat} values (s^{-1}), were automatically collected from BRENDA (108). If BRENDA did not report a k_{cat} value for an enzyme, GECKO searched for alternative k_{cat} values by reducing specificity, on the level of substrate, enzymatic activity (EC number) and organism. While 4178 out of 4753 queried enzyme activities could be matched to the full EC code, 306 of the matched activities reported in BRENDA were from *S. coelicolor.* Additionally, six k_{cat} values were manually curated, and a thorough explanation and reasoning behind these modifications are given in the **Supplemental Information**. The NAD(H)/NAD(P)H pseudo-reactions were blocked to avoid infeasible loops.

Then, separate models were created for each strain (the gene clusters for actinorhodin, undecylprodigiosin, CDA and coelimycin P1 were removed to create M1152) and for each time point by using estimated growth, uptake rates of glutamate and glucose, secretion rates of undecylprodigiosin, germicidin A and B and proteome measurements (**Supplemental Information**). These time point specific models (9 time points for M145, 8 time points for

bioRxiv preprint doi: https://doi.org/10.1101/796722; this version posted March 26, 2020. The copyright holder for this preprint (which was not certified by peer review) is the author/funder, who has granted bioRxiv a license to display the preprint in perpetuity. It is made available under aCC-BY 4.0 International license.

M1152) were used to analyse the activity in individual metabolic pathways through random sampling (65). We also created one EcSco-GEM model for each strain with a global constraint on the protein usage instead of specific protein usage, which were used for model quality control.

Continuous integration and quality control with memote

Validation and quality assessment of Sco-GEM is carried out using the test-suite in memote (42). Memote provides by default a large range of tests, which we have used to identify issues and possible improvements. The test suite reports descriptive model statistics such as the number of genes, reactions and metabolites, and also checks the presence of SBO terms and annotations, the charge and mass balance of all reactions, the network topology and find energy-generating cycles (109). Additionally, we incorporated custom tests into the memote test-suite to automatically compare predicted phenotypes with experimental data in different growth media and for different knockout mutants. The experimental growth and knockout data are extracted from (15). Memote version 0.9.12 was used in this work, and the full memote report for Sco-GEM is given in the **Supplemental Information**. As a separate evaluation, we applied the method for identifying internal and unrealistic energy-generating cycles by (110) , and no such cycles were found in Sco-GEM.

The simplest use of memote is generating snapshot reports showing the current state of the model. However, by integrating Travis CI [https://travis-ci.com/] into the gitHub repository, memote can be used to create a continuous report displaying how each commit affects the model quality.

bioRxiv preprint doi: https://doi.org/10.1101/796722; this version posted March 26, 2020. The copyright holder for this preprint (which was not certified by peer review) is the author/funder, who has granted bioRxiv a license to display the preprint in perpetuity. It is made available under aCC-BY 4.0 International license.

Random sampling, normalization and pathway analysis

Because of the huge number of reactions in the EcSco-GEM, it is challenging to sample the solution space appropriately: we have chosen to use the method provided in the Raven Toolbox 2 (37, 65), which samples the vertices of the solution space. The drawback of this method is that it will not result in a uniform sampling of the solution space. However, it is more likely to span the entire solution space and also not prone to get stuck in extremely narrow parts of the solution space, which may happen with variants of the hit-and-run algorithm (111–113). For each of the time points for each strain (17 different conditions in total) we constrained exchange reactions between 99% and 101% of the measured rates and generated 5000 random flux distributions with Gurobi as the solver. The reactions catalysed by isoenzymes were combined into the set of reactions in Sco-GEM and the reactions providing protein for each reaction. The mean of the 5000 flux distributions for each metabolic reaction was used in the following analysis.

Finally, for each of the 17 conditions, the mean fluxes were normalized by the CO_2 production rate. Then, the normalized mean fluxes were summarized for each metabolic pathway by using the curated pathway annotations, and we consider this a measure of the metabolic activity in each pathway.

Since glucose and glutamate uptake rates, as well as growth rates were significantly different in the two strains and at different time points, normalization of the data was necessary to compare flux distributions. We tested various proxies as indicators of overall metabolic activity for normalization, namely CO_2 production; the total carbon uptake from glucose and glutamate; growth rate and mean flux value. As golden standard, we compared the fluxes through individual reactions that are well documented to change in M145 in response to the

bioRxiv preprint doi: https://doi.org/10.1101/796722; this version posted March 26, 2020. The copyright holder for this preprint (which was not certified by peer review) is the author/funder, who has granted bioRxiv a license to display the preprint in perpetuity. It is made available under aCC-BY 4.0 International license.

phosphate depletion (**Figure S8**). Normalization based on CO_2 production was tested and gave similar results than the data normalized on total carbon uptake from glucose and glutamate (**Figure S8A and S8B**. The data normalized by the sum of fluxes showed similar patterns as those achieved by glucose/glutamate and CO_2-normalized data but was noisier (**Figure S8C**). Considering the huge differences in growth rate, the growth-normalized data masked any other flux patterns (**Figure S8D**). The fact that different normalizations provided similar differences in metabolic fluxes proved that the inferred changes in metabolism were not artefacts of the normalization method but represent true metabolic activity of each strain.

Strains, cultivation conditions, sampling procedures, and analyses of media components and antibiotics box

Experiments were performed using strain M145 of *S. coelicolor* A3(2) and its derivatives M1146 and M1152. The latter two are lacking the 4 major BGCs for actinorhodin (Act), undecylprodigiosin (Red), coelimycin P1 (Cpk), and calcium-dependent antibiotic (CDA), while M1152 is also carrying the pleiotropic, previously described antibiotic production enhancing mutation *rpoB* [S433L] (13, 22). All strains were kindly provided by Mervyn Bibb at John-Innes-Centre, Norwich, UK.

Triplicate cultivations of the strains were performed based on germinated spore inoculum on 1.8 L phosphate-limited medium SSBM-P, applying all routines of the optimized submerged batch fermentation strategy for *S. coelicolor* established and described before (20). All media were based on ion-free water, and all chemicals used were of analytical grade. In brief, spore batches of M145, M1146 and M1152 were generated by cultivation on soy flour-mannitol (SFM) agar plates (114), harvesting by scraping off spores and suspension

bioRxiv preprint doi: https://doi.org/10.1101/796722; this version posted March 26, 2020. The copyright holder for this preprint (which was not certified by peer review) is the author/funder, who has granted bioRxiv a license to display the preprint in perpetuity. It is made available under aCC-BY 4.0 International license.

632 in 20% (v/v) glycerol, and storage in aliquots at −80 °C. 10^9 CFU of spores of each strain were
633 germinated for 5 hours at 30 °C and 250 rpm in 250 mL baffled shake-flasks with 2 g of 3 mm
634 glass beads and 50 mL 2x YT medium (115). The germinated spores were harvested by
635 centrifugation (3200 x g, 15 °C, 5 min) and re-suspended in 5 mL ion-free water. An even
636 dispersion of the germinated spores was achieved by vortex mixing (30 s), ensuring
637 comparable inocula among biological replicas. Each bioreactor (1.8 liter starting volume
638 culture medium in a 3-liter Applikon stirred tank reactor) was inoculated with 4.5 mL
639 germinated spore suspension (corresponding to $9x10^8$ CFU). Phosphate-limited medium
640 SSBM-P (8) consisted of Na-glutamate, 55.2 g/L; D-glucose, 40 g/L; $MgSO_4$, 2.0 mM;
641 phosphate, 4.6 mM; supplemented minimal medium trace element solution SMM-TE (115),
642 8 mL/L and TMS1, 5.6 mL/L. TMS1 consisted of $FeSO_4$ x 7 H_2O, 5 g/L; $CuSO_4$ x 5 H_2O, 390
643 mg/L; $ZnSO_4$ x 7 H_2O, 440 mg/L; $MnSO_4$ x H_2O, 150 mg/L; Na_2MoO_4 x 2 H_2O, 10 mg/L; $CoCl_2$ x
644 6 H_2O, 20 mg/L, and HCl, 50 mL/L. Clerol FBA 622 fermentation defoamer (Diamond
645 Shamrock Scandinavia) was added to the growth medium before inoculation. Throughout
646 fermentations, pH 7.0 was maintained constant by automatic addition of 2 M HCl. Dissolved
647 oxygen levels were maintained at a minimum of 50% by automatic adjustment of the stirrer
648 speed (minimal agitation 325 rpm). The aeration rate was constant 0.5 L/(L x min) sterile air.
649 Dissolved oxygen, agitation speed and carbon dioxide evolution rate were measured and
650 logged on-line, while samples for the determination of cell dry weight, levels of growth
651 medium components and secondary metabolites concentrations, as well as for
652 transcriptome and proteome analysis were withdrawn throughout the fermentation trials as
653 indicated in **Figure 2B**. For transcriptome analysis, 3 × 4 ml culture sample were applied in
654 parallel onto three 0.45 µm nitrocellulose filters (Millipore) connected to vacuum. The
655 biomass on each filter was immediately washed twice with 4 ml double-autoclaved ion-free

bioRxiv preprint doi: https://doi.org/10.1101/796722; this version posted March 26, 2020. The copyright holder for this preprint (which was not certified by peer review) is the author/funder, who has granted bioRxiv a license to display the preprint in perpetuity. It is made available under aCC-BY 4.0 International license.

water pre-heated to 30 °C, before the filters were collected in a 50 ml plastic tube, frozen in liquid nitrogen and stored at -80 °C until RNA isolation. For proteome analysis, 5 ml samples were taken and centrifuged (3200 x g, 5 min, 4 °C), and the resulting cell pellets frozen rapidly at -80 °C until further processing.

Levels of phosphate were measured spectrophotometrically by using the SpectroQuant Phosphate test kit (Merck KGaA, Darmstadt, Germany) following the manufacturer's instructions after downscaling to 96-well plate format. D-glucose and L-glutamate concentrations were determined by LC-MS using suitable standards, and measured concentrations were used to estimate specific uptake and excretion rates.

Undecylprodigiosin (Red) levels were determined spectrophotometrically at 530 nm after acidified methanol extraction from the mycelium (116). To determine relative amounts of actinorhodins (determined as total blue pigments, TBP), cell culture samples were treated with KOH (final concentration 1 M) and centrifuged, and the absorbance of the supernatants at 640 nm was determined (116). Quantification of germicidin A and B was performed using targeted LC-MS analytics.

Proteomics

Sample preparation and NanoUPLC-MS analysis

Quantitative proteomics were performed using pipeline previously described (117). Mycelium pellets for proteome analysis were thawed and resuspended in the remaining liquid. 50 µL re-suspended mycelium was withdrawn and pelleted by centrifugation. 100 µL lysis buffer (4% SDS, 100 mM Tris-HCl pH 7.6, 50 mM EDTA) was added, and samples were sonicated in a water bath sonicator (Biorupter Plus, Diagenode) for 5 cycles of 30 s high power and 30 s off in ice water. Cell debris was pelleted and removed by centrifugation.

bioRxiv preprint doi: https://doi.org/10.1101/796722; this version posted March 26, 2020. The copyright holder for this preprint (which was not certified by peer review) is the author/funder, who has granted bioRxiv a license to display the preprint in perpetuity. It is made available under aCC-BY 4.0 International license.

Total protein was precipitated using the chloroform-methanol method described before (118). The pellet was dried in a vacuum centrifuge before dissolving in 0.1% RapiGest SF surfactant (Waters) at 95 °C. The protein concentration was measured at this stage using BCA method. Protein samples were then reduced by adding 5 mM DTT, followed by alkylation using 21.6 mM iodoacetamide. Then trypsin (recombinant, proteomics grade, Roche) was added at 0.1 µg per 10 µg protein. Samples were digested at 37 °C overnight. After digestion, trifluoroacetic acid was added to 0.5% followed by incubation at 37 °C for 30 min and centrifugation to remove MS interfering part of RapiGest SF. Peptide solution containing 8 µg peptide was then cleaned and desalted using STAGE-Tipping technique (119). Final peptide concentration was adjusted to 40 ng/µL using sample solution (3% acetonitrile, 0.5% formic acid) for analysis.

200 ng (5 µL) digested peptide was injected and analysed by reversed-phase liquid chromatography on a nanoAcquity UPLC system (Waters) equipped with HSS-T3 C18 1.8 µm, 75 µm X 250 mm column (Waters). A gradient from 1% to 40% acetonitrile in 110 min (ending with a brief regeneration step to 90% for 3 min) was applied. [Glu^{1}]-fibrinopeptide B was used as lock mass compound and sampled every 30 s. Online MS/MS analysis was done using Synapt G2-Si HDMS mass spectrometer (Waters) with an UDMS^{E} method set up as described in (120).

Data processing and label-free quantification

Raw data from all samples were first analysed using the vender software ProteinLynx Global SERVER (PLGS) version 3.0.3. Generally, mass spectrum data were generated using an MS^{E} processing parameter with charge 2 lock mass 785.8426, and default energy thresholds. For protein identification, default workflow parameters except an additional acetyl in N-terminal

bioRxiv preprint doi: https://doi.org/10.1101/796722; this version posted March 26, 2020. The copyright holder for this preprint (which was not certified by peer review) is the author/funder, who has granted bioRxiv a license to display the preprint in perpetuity. It is made available under aCC-BY 4.0 International license.

variable modification were used. Reference protein database was downloaded from GenBank with the accession number NC_003888.3. The resulted dataset was imported to ISOQuant version 1.8 (120) for label-free quantification. Default high identification parameters were used in the quantification process. TOP3 result was converted to PPM (protein weight) and send to the modelers and others involved in interpreting the data (**Data Set S1, Tab 14**).

TOP3 quantification was filtered to remove identifications meet these two criteria: 1. identified in lower than 70% of samples of each strain and 2. sum of TOP3 value less than 1×10^5. Cleaned quantification data was further subjected to DESeq2 package version 1.22.2 (29) and PCA was conducted after variance stabilizing transformation (vst) of normalized data.

Transcriptomics

RNA extraction and quality control

Bacteria were lysed using RNAprotect Bacteria (Qiagen) and following the manufacturer´s instruction. Briefly, filters containing bacteria were incubated with 4 ml of RNAprotect Bacteria reagent. After centrifugation, resulting samples were lysed using 500 µl of TE buffer (10 mM Tris·Cl, 1 mM EDTA, pH 8.0) containing 15 mg/ml lysozyme using 150-600 µm diameter glass beads (Sigma) agitated at 30 Hz for 5 minutes in the TissueLyser II (Qiagen).

Total RNA was extracted using RNeasy mini kit (Qiagen) and 700 µl of the resulting lysate complemented with 470 µl of absolute ethanol. RNAase-free DNase set (Qiagen) and centrifugation steps were performed to prevent DNA and ethanol contamination. Elution was performed using 30 µl of RNase-free water and by reloading the eluate on the column to improve the RNA yield. The RNA concentration was measured using Qubit RNA BR Assay Kit

bioRxiv preprint doi: https://doi.org/10.1101/796722; this version posted March 26, 2020. The copyright holder for this preprint (which was not certified by peer review) is the author/funder, who has granted bioRxiv a license to display the preprint in perpetuity. It is made available under aCC-BY 4.0 International license.

(ThermoFisher Scientific), RNA purity was assessed using A260/A280 and A260/A230 ratio using the Nano Drop ND-1000 Spectrophotometer (PEQLAB). RNA Integrity Number was estimated using RNA 6000 Nano Kit (Agilent) and the Bioanalyzer 2100 (Agilent).

Library preparation and sequencing

A total of 1 µg of total RNA was subjected to rRNA depletion using Ribo-Zero rRNA Removal Kit Bacteria (Illumina). The cDNA libraries were constructed using the resulting tRNA and the NEBNext Ultra II Directional RNA Library Prep Kit (NEB). Libraries were sequenced as single-reads (75 bp read length) on an Illumina NextSeq500 platform at a depth of 8–10 million reads each.

RNA-seq data assessment and analysis

Sequencing statistics including the quality per base and adapter content assessment of resulting transcriptome sequencing data were conducted with FastQC v0.11.5 (121). All reads mappings were performed against the reference strain of *Streptomyces coelicolor A3(2)* (RefSeq ID NC_003888.3). The mappings of all samples were conducted with HISAT2 v2.1.0 (122). As parameters, spliced alignment of reads was disabled, and strand-specific information was set to reverse complemented (HISAT2 parameter --no-spliced-alignment and --rna-strandness "R"). The resulting mapping files in SAM format were converted to BAM format using SAMtools v1.6 (123). Mapping statistics, including strand specificity estimation, percentage of mapped reads and fraction exonic region coverage, were conducted with the RNA-seq module of QualiMap2 v2.2.2-dev (124). Gene counts for all samples were computed with featureCounts v1.6.0 (28) based on the annotation of the respective reference genome, where the selected feature type was set to transcript records (featureCounts parameter -t transcript).

bioRxiv preprint doi: https://doi.org/10.1101/796722; this version posted March 26, 2020. The copyright holder for this preprint (which was not certified by peer review) is the author/funder, who has granted bioRxiv a license to display the preprint in perpetuity. It is made available under aCC-BY 4.0 International license.

Normalization and differential gene expression

Raw count files were imported into Mayday SeaSight (125) for common, time-series-wide normalization. For this, the raw counts of all biological replicates of one strain across the time-series were log2-transformed (with pseudocount of +1 for the genes with zero counts) and then quantile-normalized. To make the two normalized time-series data of M154 and M1152 comparable, they were again quantile-normalized against each other. The normalized RNA-seq data are provided in **Data Set S1, Tab 15.**

Differentially expressed genes were identified by ANOVA using Orange (v3.2) and the bioinformatic toolkit (v), with FDR of <0.01 and a minimal fold enrichment >1 for at least one aligned time point. Genes with low expression (log2 < 5 for both strains and time points) were not considered for further analysis. The differentially expressed genes were subsequently scaled to the expression average and clustered by K-means. Visualization of genes and clusters were performed in python (v3.7) with matplotlib (v3.1.1). For this, the time-series of M145 and M1152 were aligned such that in the visual representation, the expression profiles of the two strains are aligned relative to the time point of phosphate depletion. Both DAVID (126, 127) and the string database (128) was used to evaluate the function of each cluster, identifying overrepresentation of function groups based on GO annotation or text mining. Identified differential clusters or regulons were extracted from literature and plotted (**Data Set S1, Tab 5; Figure S7**).

bioRxiv preprint doi: https://doi.org/10.1101/796722; this version posted March 26, 2020. The copyright holder for this preprint (which was not certified by peer review) is the author/funder, who has granted bioRxiv a license to display the preprint in perpetuity. It is made available under aCC-BY 4.0 International license.

Data and Software Availability

Model repository

The model is hosted and developed in an open repository on GitHub: https://github.com/SysBioChalmers/Sco-GEM. Here, the latest version of the Sco-GEM is available in both YAML and SBML level 3 Version 1. Additionally, users can see all details of the model reconstruction and contribute to further model development by posting issues or suggest changes. This should encourage further, incremental development of Sco-GEM by the community.

Proteome data

The proteomics data have been deposited to the ProteomeXchange Consortium via the PRIDE (129) partner repository with the dataset identifier PXD013178 and 10.6019/PXD013178. Normalized proteome data is also available in **Data Set S1, Tab 14.**

Transcriptomics data

All high-throughput sequencing data have been deposited in NCBI's Gene Expression Omnibus and are accessible under accession number GSE132487 (M145) and GSE132488 (M1152). Normalized counts are also found in **Data Set S1, Tab 15.**

Author contributions

Conceptualization, E.K., E.A., A.W., S.S., A.S.Y. and T.K. Methodology and software, E.K., S.S., A.S.Y. and T.K. Validation and formal analysis, C.D., K.N., D.V.D., S.S., T.K., E.K. Investigation, T.K., A.W., S.S., E.K. Data curation, S.S., T.K. Writing - original draft, S.S., T.K., D.V.D., C.D., K.N. Writing – review & editing, all authors. Visualization, S.S., E.K., C.D., D.V.D. Supervision, A.W., E.A., E.K., G.W. Project administration, A.W. Funding acquisition: A.W., E.K., E.A., G.W.

bioRxiv preprint doi: https://doi.org/10.1101/796722; this version posted March 26, 2020. The copyright holder for this preprint (which was not certified by peer review) is the author/funder, who has granted bioRxiv a license to display the preprint in perpetuity. It is made available under aCC-BY 4.0 International license.

Acknowledgements

The authors would like to acknowledge Bogdan I. Florea of Leiden University, Leiden, Netherlands, for running and monitoring the proteome measurements, and the bio-organic synthesis group at Leiden University for providing the opportunity to use their instrumentation. The authors would also like to acknowledge co-workers at SINTEF Industry, Trondheim, Norway: Ingemar Nærdal, Anna Lewin and Kari Hjelen for running the batch fermentations and Anna Nordborg, Janne Beate Øiaas and Tone Haugen for performing offline analyses and the germicidin analytics. The RNA-Seq sequencing was carried out by c.ATG, Tübingen, Germany.

This study was conducted in the frame of ERA-net for Applied Systems Biology (ERA-SysAPP) project SYSTERACT and the project INBioPharm of the Centre for Digital Live Norway (Research Council of Norway grant no. 248885), with additional support of SINTEF internal funding. The authors declare no conflict of interest.

bioRxiv preprint doi: https://doi.org/10.1101/796722; this version posted March 26, 2020. The copyright holder for this preprint (which was not certified by peer review) is the author/funder, who has granted bioRxiv a license to display the preprint in perpetuity. It is made available under aCC-BY 4.0 International license.

Figures

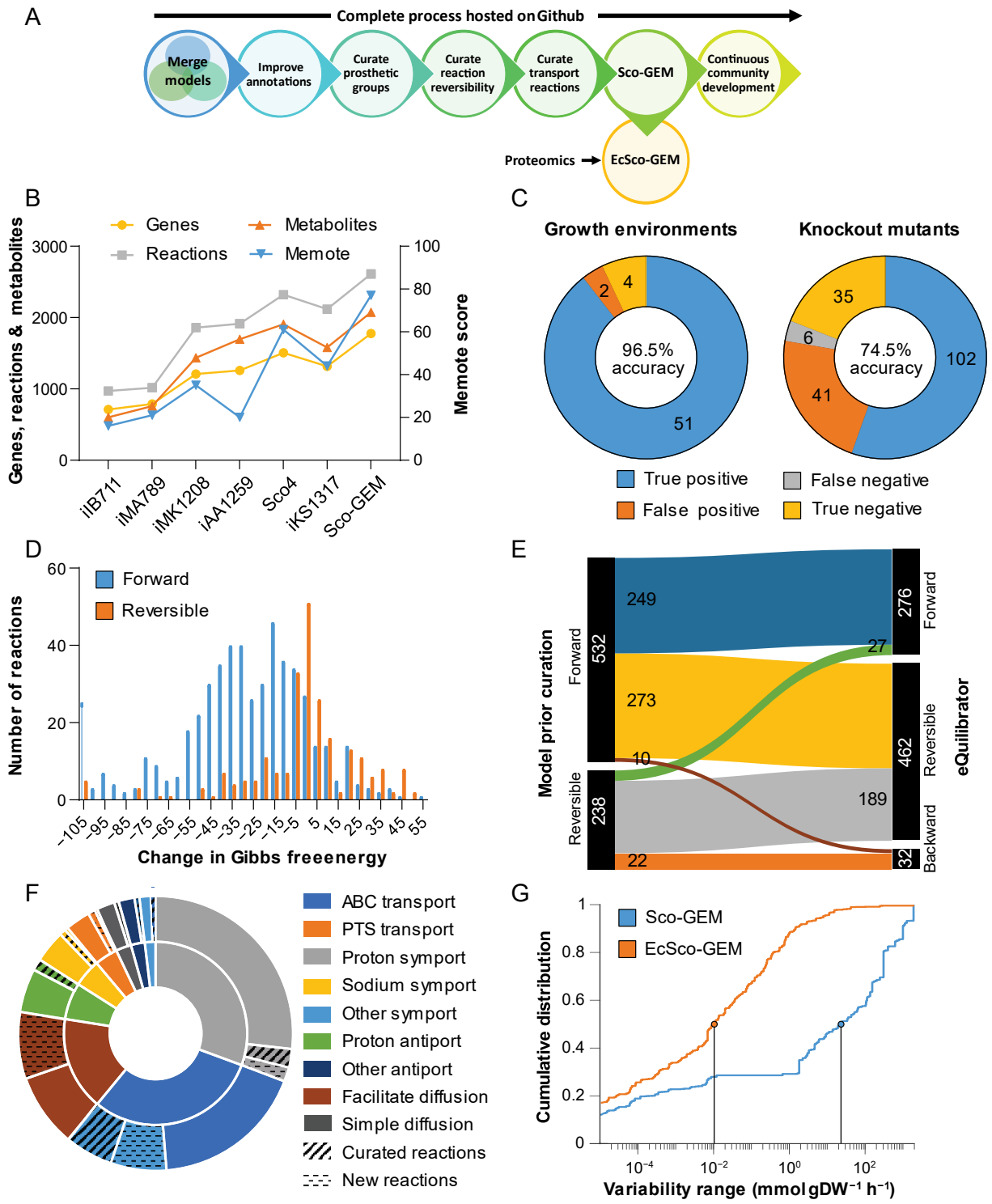

Figure 1: Sco-GEM development and analysis. A) Schematic overview of the various steps in the Sco-GEM reconstruction process. B) The overall memote score and number of genes, reactions and metabolites for the 7 published *S. coelicolor* GEMs. C) Assessment of the model

bioRxiv preprint doi: https://doi.org/10.1101/796722; this version posted March 26, 2020. The copyright holder for this preprint (which was not certified by peer review) is the author/funder, who has granted bioRxiv a license to display the preprint in perpetuity. It is made available under aCC-BY 4.0 International license.

quality by comparing *in vivo* observations with *in silico* predictions across in total 241 tests: accuracy = 0.80; sensitivity = 0.96; specificity = 0.48; Matthews Correlation Coefficient = 0.53. D) The change in Gibbs free energy for 770 reactions that were annotated as either reversible or forward irreversible in the model prior curation of reaction reversibility. The histogram is truncated at -105 kJ/mol, and more negative values are assigned to the leftmost bin. E) Analysis and comparison of the directionality and reversibility of reactions prior curation and the direction inferred from the change in Gibbs free energy as estimated by eQuilibrator. F) Overview of the 369 transport reactions included in Sco-GEM, whereof 42 were curated and 65 added during this work. The inner ring categorizes the reactions into 9 different subgroups, while the outer ring displays the amount of curated and added reactions within each category. G) Comparison of cumulative flux variability distributions, demonstrating that the incorporation of kinetic coefficients in EcSco-GEM greatly constrains the solution space.

bioRxiv preprint doi: https://doi.org/10.1101/796722; this version posted March 26, 2020. The copyright holder for this preprint (which was not certified by peer review) is the author/funder, who has granted bioRxiv a license to display the preprint in perpetuity. It is made available under aCC-BY 4.0 International license.

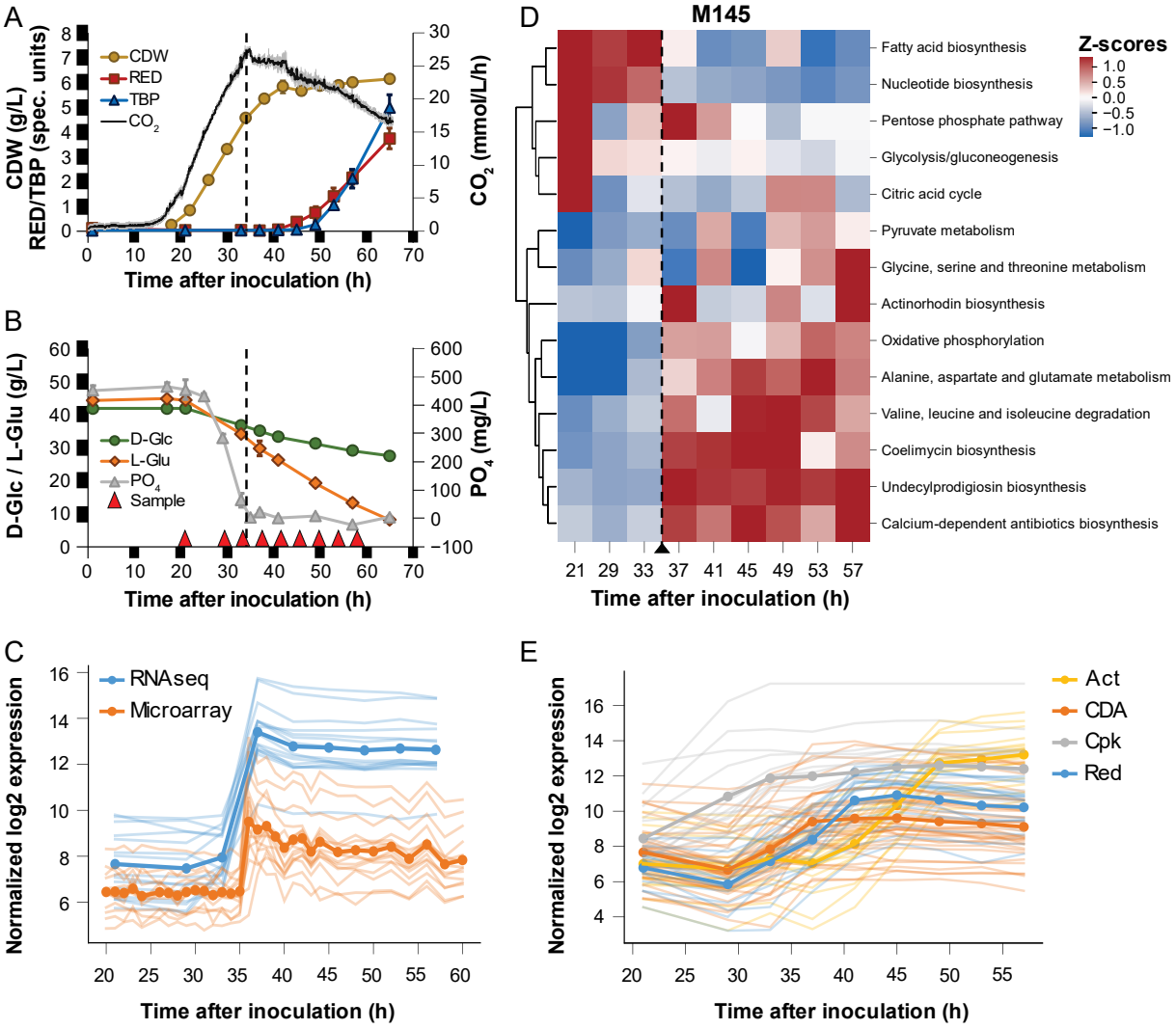

Figure 2: Batch cultivation of *S. coelicolor* M145 and the effect of phosphate depletion. Compounds produced (A) and consumed (B) during batch fermentation of *S. coelicolor* M145. Time points for sampling for transcriptome and proteome analysis are indicated with red triangles. The dashed vertical line indicates when phosphate in the medium has been depleted. Error bars are standard deviations of three biological replicates. CDW, Cell Dry Weight; Red, undecylprodigiosin; TBP, Total Blue Pigments/actinorhodins; CO_2 volume corrected respiration; D-Glc, D-glucose; L-Glu, L-glutamate; PO_4, phosphate. C) Comparison of previously published microarray data (8) and RNA-seq data (this study) for genes previously found to respond to phosphate depletion (8). D) Clustered heatmap of CO_2-normalized Z-scores for each of the top 10 varying pathways plus the pathways for the 4 major BGCs in

bioRxiv preprint doi: https://doi.org/10.1101/796722; this version posted March 26, 2020. The copyright holder for this preprint (which was not certified by peer review) is the author/funder, who has granted bioRxiv a license to display the preprint in perpetuity. It is made available under aCC-BY 4.0 International license.

832 M145, as revealed by simulations with the proteomics-integrated EcSco-GEM model. The
833 dashed vertical line indicates the time point of the metabolic switch. E) RNA-seq data of the 4
834 major BGCs show the onset of biosynthesis of actinorhodin (Act), calcium-dependent
835 antibiotic (CDA), coelimycin P1 (Cpk) and undecylprodigiosin (Red) at different time points
836 during the batch fermentations of M145.

837

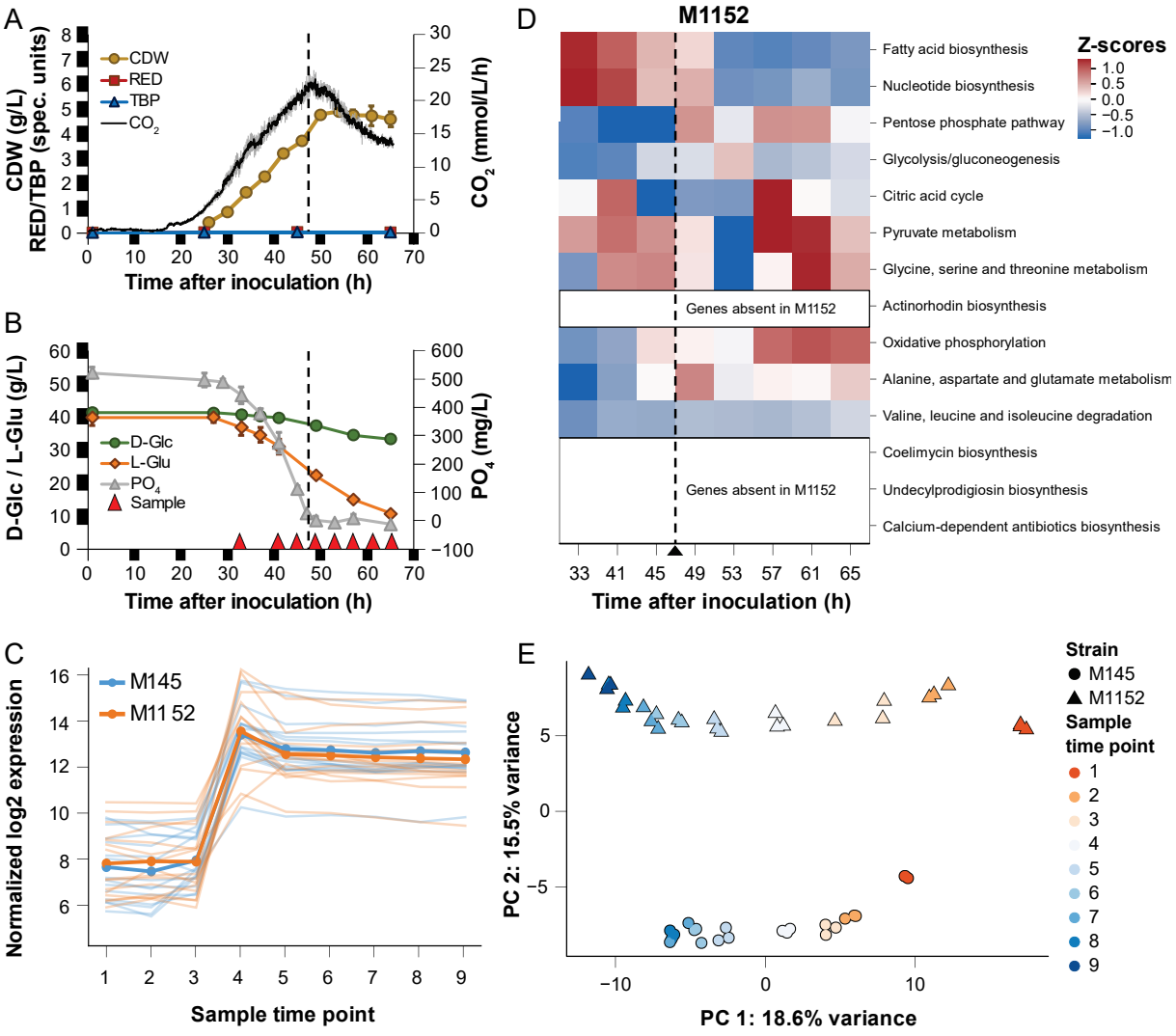

838

839 **Figure 3: Batch cultivation of *S. coelicolor* M1152.** Compounds produced (A) and consumed
840 (B) during batch fermentation of *S. coelicolor* M1152. Time points for sampling for
841 transcriptome and proteome analysis are indicated with red triangles. The dashed vertical line

bioRxiv preprint doi: https://doi.org/10.1101/796722; this version posted March 26, 2020. The copyright holder for this preprint (which was not certified by peer review) is the author/funder, who has granted bioRxiv a license to display the preprint in perpetuity. It is made available under aCC-BY 4.0 International license.

indicates when phosphate in the medium has been depleted. Error bars are standard deviations of three biological replicates. CDW, Cell Dry Weight; Red, undecylprodigiosin; TBP, Total Blue Pigments/actinorhodins; CO_2, volume corrected respiration; D-Glc, D-glucose; L-Glu, L-glutamate; PO_4, phosphate. C) Alignment of sample time points of M145 and M1152 cultivations based on the expression profiles of genes that were earlier found to respond to phosphate depletion in respect to the metabolic switch (8). D) Clustered heatmap of proteomics data for M145 (triangles) and M1152 (circles), for each time-point and culture. The first principal component separates the time points, while the second principal component separates the two strains. E) CO_2-normalized Z-scores of pathway fluxes predicted by EcSco-GEM for 10 of the most varying pathways in M145 and M1152. The data for M145 (**Figure 2D**) and M1152 are standardized together to make values and colours comparable. E) Principle component analysis of the proteomics data for M145 (triangles) and M1152 (circles), for each time-point and culture. The first principal component separates the time points while the second principal component separates the two strains.

bioRxiv preprint doi: https://doi.org/10.1101/796722; this version posted March 26, 2020. The copyright holder for this preprint (which was not certified by peer review) is the author/funder, who has granted bioRxiv a license to display the preprint in perpetuity. It is made available under aCC-BY 4.0 International license.

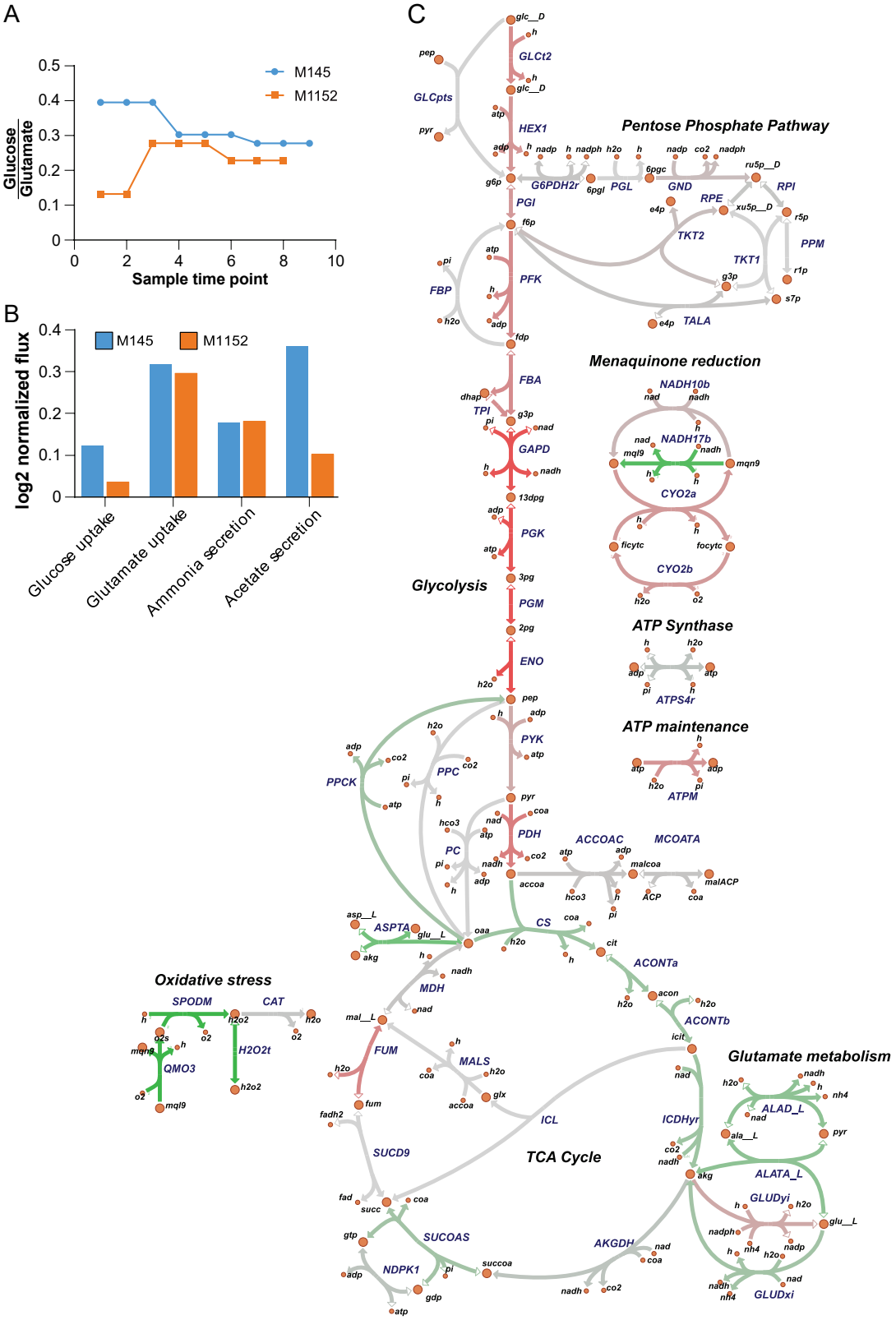

Figure 4: Predicted carbon fluxes in M145 and M1152. A) The ratio between estimated uptake rates of glucose and glutamate showing that M1152 acquires a smaller part of its carbon from glucose compared to M145. B) Roughly half of the nitrogen from glutamate is excreted as

bioRxiv preprint doi: https://doi.org/10.1101/796722; this version posted March 26, 2020. The copyright holder for this preprint (which was not certified by peer review) is the author/funder, who has granted bioRxiv a license to display the preprint in perpetuity. It is made available under aCC-BY 4.0 International license.

ammonium (both strains), while higher uptake of glucose in M145 leads to more excretion of acetate. C) Comparison of predicted fluxes for the second sampling time points for M145 and M1152, i.e. after 29 and 41 hours, respectively. The second time point for each strain was chosen because the estimated uptake rates are more reliable than the first time point. The strength of the colour of the lines correspond to the flux difference between the strains; green reactions have higher flux in M1152, and red reactions have higher flux in M145. Note the reduced biomass-specific uptake rate of glucose and increased oxidative stress in M1152.

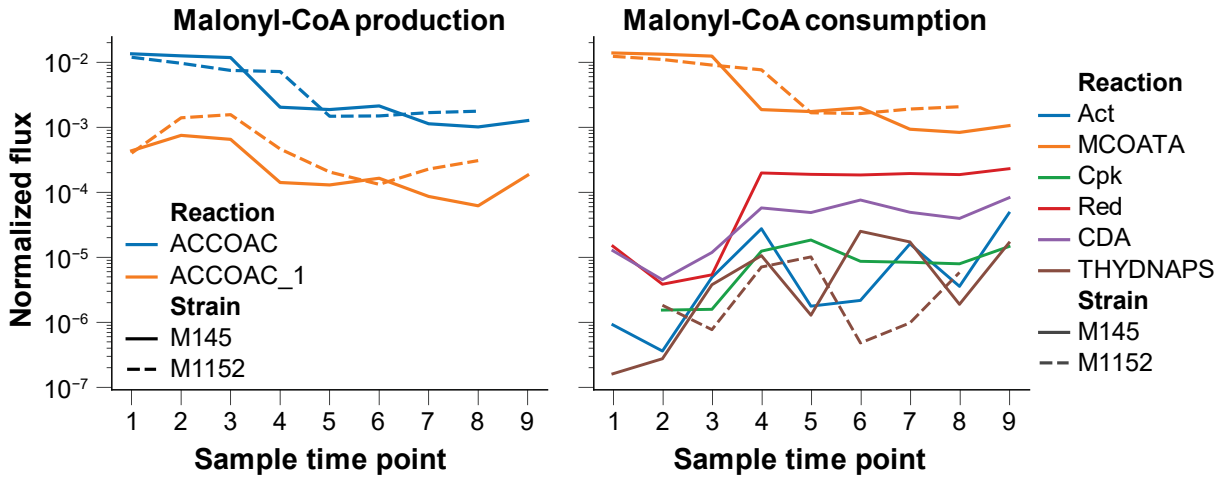

Figure 5: Production and consumption of malonyl-CoA as the branching point between fatty acid biosynthesis and production of polyketides. From EcSco-GEM predictions, a reduced malonyl-CoA production (left panel) by both acetyl-CoA carboxylase (ACCOAT; blue) and acetyl-CoA carboxytransferase (ACCOAT_1; orange) is observed in both strains. Most of the malonyl-CoA is consumed by fatty acid biosynthesis through malonyl-CoA-ACP transacylase (MCOATA), even after metabolic switching, and this consumption balances the malonyl-CoA production. The other main sinks for malonylmalonyl-CoA are the pathways encoded by the 4 major BGCs (Act, Cpk, Red and CDA) in addition to biflaviolin synthase (THYDNAPS).

bioRxiv preprint doi: https://doi.org/10.1101/796722; this version posted March 26, 2020. The copyright holder for this preprint (which was not certified by peer review) is the author/funder, who has granted bioRxiv a license to display the preprint in perpetuity. It is made available under aCC-BY 4.0 International license.

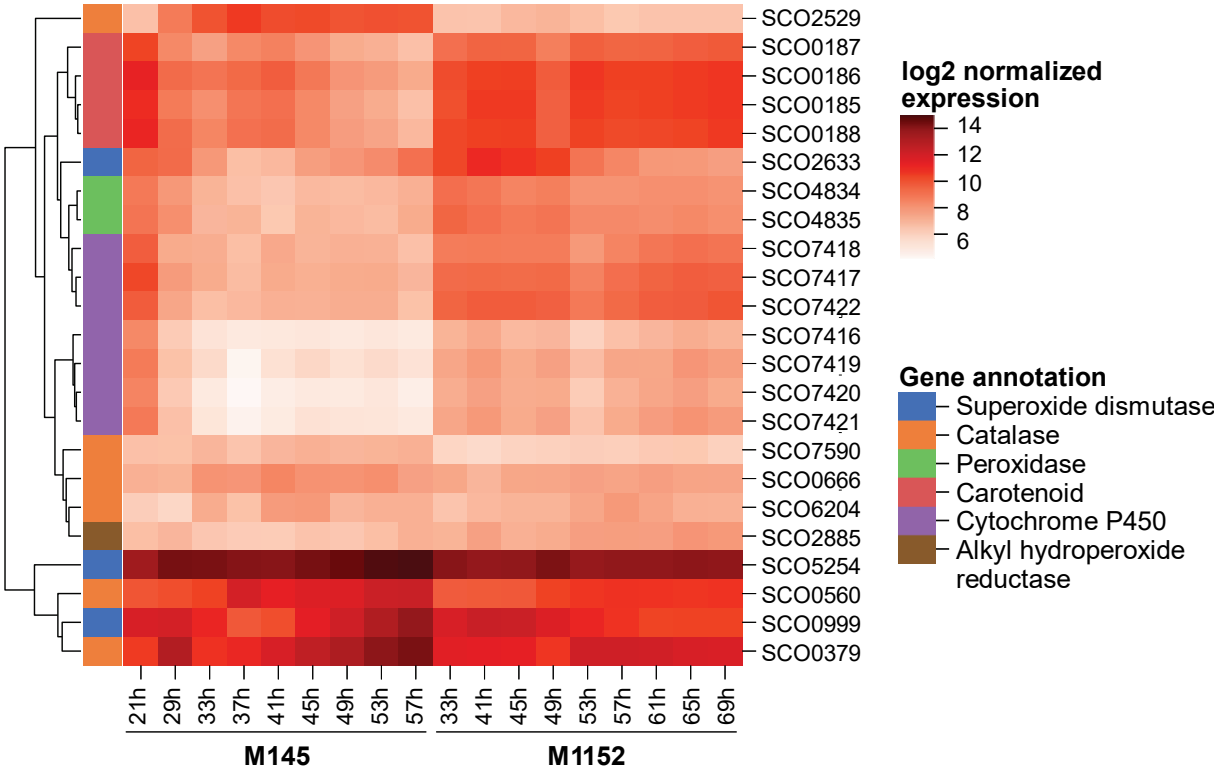

Figure 6: Heatmap displaying log-transformed RNA-seq data of genes associated with oxidative stress. Included are genes related to oxidative stress either present in Sco-GEM or within the 499 differentially expressed genes. A general upregulation in M1152 and the first time point of M145 is observed.

bioRxiv preprint doi: https://doi.org/10.1101/796722; this version posted March 26, 2020. The copyright holder for this preprint (which was not certified by peer review) is the author/funder, who has granted bioRxiv a license to display the preprint in perpetuity. It is made available under aCC-BY 4.0 International license.

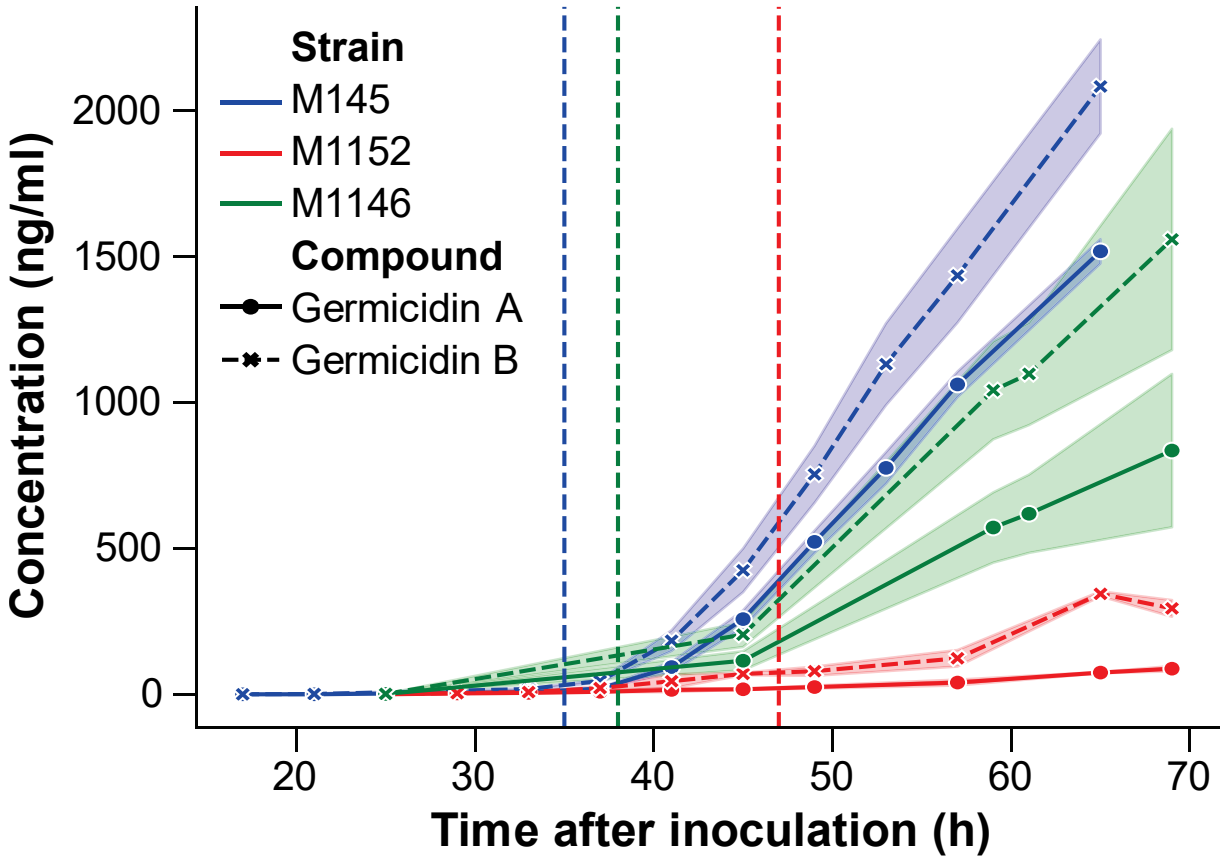

Figure 7: Concentrations of germicidin A and B produced by M145, M1146 and M1152. The shaded regions display the uncertainty range (± 1 standard deviation) based on three replicate cultivations. Germicidin production rates after the metabolic switch (in ng ml^{-1} $hour^{-1}$) are: 41.4 (A) and 75.5 (B) for M145; 30.2 (A) and 56.4 (B) for M1146; 3.3 (A) and 13.3 (B) for M1152. Note that the growth rate is different between the strains, displayed by the vertical lines representing phosphate depletion at 35, 38 and 47 hours for M145, M1146 and M1152, respectively.

Supplemental Figures

Figure S1: Reaction subsystems and origin. The number of reactions in Sco-GEM in each of the 15 subsystems, and from which model they originate from. The other reactions (orange) are added during reconstruction of Sco-GEM.

bioRxiv preprint doi: https://doi.org/10.1101/796722; this version posted March 26, 2020. The copyright holder for this preprint (which was not certified by peer review) is the author/funder, who has granted bioRxiv a license to display the preprint in perpetuity. It is made available under aCC-BY 4.0 International license.

Figure S2: Gene clusters associated with metabolic switch. RNA-seq (left column) and proteomics (right column) from M145 of the 8 gene clusters associated with the metabolic switch as previously identified (8). The 8 clusters are: A) genes related to ribosomal proteins; B) genes related to nitrogen metabolism; C) Cpk gene cluster; D) genes related to development; E) genes upregulated in response to phosphate depletion; F) genes involved in synthesis of phosphate-free polymers; G) Act gene cluster; H) Red gene cluster

Figure S3: Log-transformed expression levels of genes related to nitrogen metabolism. The glutamate import (SCO5774-5777), the glutamate sensing system *gluR-gluK* (SCO5778 and SCO57779), *glnR* (SCO4159) and *glnA* (SCO2198) are downregulated subsequent to phosphate depletion. We also observe that the first time point in M145 is very different from all other samples.

Figure S4: Clustered heatmaps of Z-score based on CO_2-normalized sum of fluxes of all pathways standardized within each pathway and separated into different subsystems / parts of the metabolism. A) Central carbon metabolism. B) Amino acid metabolism. C) Metabolism of vitamins and cofactors. D) Pathways of Biosynthetic gene clusters. E) Lipid metabolism. F) Oxidative stress. G) Degradation of toxic compounds. H) All other pathways. For all panels only pathway with a minimum flux of 1e-8 mmol (g DW)$^{-1}$ h^{-1} were included.

Figure S5: **RNA-seq, proteome and flux prediction of specific gene clusters and reactions.** A) EcSco-GEM predicts that the flux through citrate synthase (CS) and isocitrate dehydrogenase (ICDHyr) increases at later time points in M145, effectively increasing the shuttling of acetyl-CoA into the TCA cycle. B) Log2 normalized expression data of genes involved in oxidative phosphorylation indicate an increasing expression at later time points, while overall expression in M1152 is higher than in M145. C-H) Comparison of log2 normalized expression

bioRxiv preprint doi: https://doi.org/10.1101/796722; this version posted March 26, 2020. The copyright holder for this preprint (which was not certified by peer review) is the author/funder, who has granted bioRxiv a license to display the preprint in perpetuity. It is made available under aCC-BY 4.0 International license.

data as calculated with (log2 M145)-log2(M1152), where positive values indicate upregulation in M145 relative to M1152, and vice versa for negative values. C) Increased expression of genes of the afsR regulon in M145, while no significant difference in expression is observed for (D) scbR regulon; (E) adpA regulon; (F) argR regulon; (G) genes induced by ppGPP; and (H) genes repressed by ppGpp.

Figure S6: Analysis of transcriptome data of genes. A) Unsupervised clustering (k-means) of significantly changed genes into 7 clusters: the first three (clusters 1-3) are upregulated in M1152, while the last four (clusters 4-7) are upregulated from the beginning or at later time points in M145. B-D) Comparison of log2 normalized expression data as calculated with (log2 M145)-log2(M1152), where positive values indicate upregulation in M145 relative to M1152, and vice versa for negative values. B) Genes in the SoxR regulon are reducing expression in M1152 at later time points. C) Almost all genes in the ATP-synthase cluster are up-regulated in M1152 after the first time point. D) Also, the transcription of ribosomal protein genes after the metabolic switch is increased in M1152 compared to M145. E) Batch cultivation of *S. coelicolor* M1146. Error bars are standard deviations of three biological replicates. CDW, Cell Dry Weight; CO_2 volume corrected respiration; PO_4, phosphate.

Figure S7: Gene Ontology enrichment analysis of the 7 clusters identified in the 499 differentially expressed genes, categorized by function into four clustered heatmaps.

Each heatmap shows the p-value for the enrichment of each GO-process. A) Genes related to reactive oxygen species, the ribosome or development process and cell wall formation. B) Oxireductase and iron / metal ion homeostasis. C) Regulation, biosynthesis and metabolism related to RNA and DNA. D) All other GO-annotations. E) This color palette is the legend for the column colors on top of each heatmap which displays which of the seven clusters each

bioRxiv preprint doi: https://doi.org/10.1101/796722; this version posted March 26, 2020. The copyright holder for this preprint (which was not certified by peer review) is the author/funder, who has granted bioRxiv a license to display the preprint in perpetuity. It is made available under aCC-BY 4.0 International license.

gene belongs to. The red palette covers cluster 1-3 (upregulated in M1152), while the blue palette covers cluster 4-7 (upregulated in M145). Note that no GO-processes were enriched for the genes in cluster 2.

Figure S8: Comparison of normalization methods of randomly sampled fluxes. Heatmap showing mean flux values normalized by A) total carbon uptake from glucose and glutamate, B) CO_2 production, C) sum of all fluxes and D) growth rate. Because the mean flux values in these reactions are different by several orders of magnitude, we display the data as standardized values (for each reaction).

Other Supplemental material

Supplemental Information: The Memote report of Sco-GEM, the protocols for Sco-GEM and EcSco-GEM development and a detailed description of estimation of rates from batch fermentation data.

Data Set S1

Tab 1: Detailed overview of the script performing the reconstruction of Sco-GEM.

Tab 2: Comparison of the new biomass reaction in Sco-GEM with the biomass reaction in iAA1259.

Tab 3: Reversibility prior update, calculated change in Gibbs free energy and standard deviation of the calculated change in Gibbs free energy of 770 reactions in Sco-GEM.

Tab 4: Overview of all transport reactions added or curated during the process of Sco-GEM model development, and the metabolites added along with the new transport reactions.

bioRxiv preprint doi: https://doi.org/10.1101/796722; this version posted March 26, 2020. The copyright holder for this preprint (which was not certified by peer review) is the author/funder, who has granted bioRxiv a license to display the preprint in perpetuity. It is made available under aCC-BY 4.0 International license.

Tab 5: Genes present in the 7 clusters identified with K-Means clustering of the differentially expressed genes.

Tab 6: Sco4 ID, name and Sco-GEM ID of the reactions added from Sco4 to Sco-GEM.

Tab 7: Sco4 ID, name and Sco-GEM ID of the metabolites added from Sco4 to Sco-GEM

Tab 8: Reaction ID, name and gene annotation of reactions added from iAA1259 to Sco-GEM.

Tab 9: List of reactions modified according to iAA1259.

Tab 10: Metabolite ID and name of metabolites added from Sco4 to Sco-GEM.

Tab 11: List of SBO terms used in Sco-GEM

Tab 12: Single, pair and triplets of reactions which reduced model accuracy, in total 56 different reactions. The reversibility of these reactions was not changed according to the predicted change in Gibbs free energy.

Tab 13: Manual curation of the reversibility of the 82 reactions involving ATP predicted to be reversible by eQuilibrator.

Tab 14: Normalized proteome data for M145 and M1152. M145 is cultivated in F516-F518, while M1152 is cultivated in F519, F521, F522. Re-index IDs corresponds to the strain, fermentation-number (F516-F522), a unique number describing the experiment, and a numbering of the time points from 1 to 9 (P1-P9). I.e. the Re-indexed ID M145_F516_P2 represents the second timepoint of fermentation 516 with the strain M145. In the original IDs (row below) the P-number represents time after inoculation (in hours).

bioRxiv preprint doi: https://doi.org/10.1101/796722; this version posted March 26, 2020. The copyright holder for this preprint (which was not certified by peer review) is the author/funder, who has granted bioRxiv a license to display the preprint in perpetuity. It is made available under aCC-BY 4.0 International license.

Tab 15: Normalized RNA-seq data for all six fermenters. M145 is cultivated in F516-F518, while M1152 is cultivated in F519, F521, F522. Re-index IDs corresponds to the strain, fermentation-number (F516-F522), a unique number describing the experiment, and a numbering of the time points from 1 to 9 (P1-P9). I.e. the Re-indexed ID M145_F516_P2 represents the second timepoint of fermentation 516 with the strain M145. In the original IDs (row below) the P-number represents time after inoculation (in hours).

Tab 16: List of genes within each cluster known to be associated with the metabolic switch.

References

1. Hopwood, David A. 2007. Streptomyces in nature and medicine: the antibiotic makers. Oxford University Press, USA.

2. Hahn J-S, Oh S-Y, Roe J-H. 2002. Role of OxyR as a Peroxide-Sensing Positive Regulator in Streptomyces coelicolor A3(2). Journal of Bacteriology 184:5214–5222.

3. Hutchings MI, Hoskisson PA, Chandra G, Buttner MJ. 2004. Sensing and responding to diverse extracellular signals? Analysis of the sensor kinases and response regulators of Streptomyces coelicolor A3(2). Microbiology, 150:2795–2806.

4. Nothaft H, Rigali S, Boomsma B, Swiatek M, McDowall KJ, van Wezel GP, Titgemeyer F. 2010. The permease gene nagE2 is the key to N-acetylglucosamine sensing and utilization in Streptomyces coelicolor and is subject to multi-level control. Molecular Microbiology 75:1133–1144.

bioRxiv preprint doi: https://doi.org/10.1101/796722; this version posted March 26, 2020. The copyright holder for this preprint (which was not certified by peer review) is the author/funder, who has granted bioRxiv a license to display the preprint in perpetuity. It is made available under aCC-BY 4.0 International license.

5. Rigali S, Titgemeyer F, Barends S, Mulder S, Thomae AW, Hopwood DA, van Wezel GP. 2008. Feast or famine: the global regulator DasR links nutrient stress to antibiotic production by Streptomyces. EMBO reports 9:670–675.

6. Sola-Landa A, Rodríguez-García A, Franco-Domínguez E, Martín JF. 2005. Binding of PhoP to promoters of phosphate-regulated genes in Streptomyces coelicolor: identification of PHO boxes. Molecular Microbiology 56:1373–1385.

7. Chandra G, Chater KF. 2014. Developmental biology of Streptomyces from the perspective of 100 actinobacterial genome sequences. FEMS Microbiol Rev 38:345–379.

8. Nieselt K, Battke F, Herbig A, Bruheim P, Wentzel A, Jakobsen ØM, Sletta H, Alam MT, Merlo ME, Moore J, Omara WA, Morrissey ER, Juarez-Hermosillo MA, Rodríguez-García A, Nentwich M, Thomas L, Iqbal M, Legaie R, Gaze WH, Challis GL, Jansen RC, Dijkhuizen L, Rand DA, Wild DL, Bonin M, Reuther J, Wohlleben W, Smith MC, Burroughs NJ, Martín JF, Hodgson DA, Takano E, Breitling R, Ellingsen TE, Wellington EM, Kolter R, Siegele D, Tormo A, Hesketh A, Bucca G, Laing E, Flett F, Hotchkiss G, Smith C, Chater K, Hesketh A, Chen W, Ryding J, Chang S, Bibb M, Huang J, Lih C, Pan K, Cohen S, Lian W, Jayapal K, Charaniya S, Mehra S, Glod F, Kyung Y, Sherman D, Hu W, Strauch E, Takano E, Baylis H, Bibb M, DeRisi J, Iyer V, Brown P, Reuther J, Wohlleben W, Fink D, Weissschuh N, Reuther J, Wohlleben W, Engels A, Tiffert Y, Supra P, Wurm R, Wohlleben W, Wagner R, Reuther J, Pawlik K, Kotowska M, Chater K, Kuczek K, Takano E, Takano E, Chakraburtty R, Nihira T, Yamada Y, Bibb M, Takano E, Kinoshita H, Mersinias V, Bucca G, Hotchkiss G, Nihira T, Smith C, Bibb M, Wohlleben W, Chater K, Kotowska M, Pawlik K, Smulczyk-Krawczyszyn A, Bartosz-Bechowski H, Kuczek K, Claessen D, Rink R, Jong W de, Siebring

bioRxiv preprint doi: https://doi.org/10.1101/796722; this version posted March 26, 2020. The copyright holder for this preprint (which was not certified by peer review) is the author/funder, who has granted bioRxiv a license to display the preprint in perpetuity. It is made available under aCC-BY 4.0 International license.

J, Vreugd P de, Boersma F, Dijkhuizen L, Wosten H, Bibb M, Molle V, Buttner M, Ryding N, Kelemen G, Whatling C, Flardh K, Buttner M, Chater K, Ohnishi Y, Seo J, Horinouchi S, Sola-Landa A, Moura R, Martín J, Sola-Landa A, Rodríguez-García A, Franco-Domínguez E, Martín J, Rodríguez-García A, Barreiro C, Santos-Beneit F, Sola-Landa A, Martín J, Sola-Landa A, Rodríguez-García A, Apel A, Martín J, Feitelson J, Malpartida F, Hopwood D, Hallam S, Malpartida F, Hopwood D, Takano E, Gramajo H, Strauch E, Andres N, White J, Bibb M, Kieser T, Bibb M, Buttner M, Chater K, Hopwood D, Bystrykh L, Fernandez-Moreno M, Herrema J, Malpartida F, Hopwood D, Dijkhuizen L, Irizarry R, Bolstad B, Collin F, Cope L, Hobbs B, Speed T, Ihaka R, Gentleman R, Dietzsch J, Gehlenborg N, Nieselt K. 2010. The dynamic architecture of the metabolic switch in Streptomyces coelicolor. BMC Genomics 11:10.

9. Thomas L, Hodgson DA, Wentzel A, Nieselt K, Ellingsen TE, Moore J, Morrissey ER, Legaie R, STREAM Consortium TS, Wohlleben W, Rodríguez-García A, Martín JF, Burroughs NJ, Wellington EMH, Smith MCM. 2012. Metabolic switches and adaptations deduced from the proteomes of Streptomyces coelicolor wild type and phoP mutant grown in batch culture. Molecular & cellular proteomics : MCP 11:M111.013797.

10. Bentley SD, Chater KF, Cerdeño-Tárraga A-MA-M, Challis GL, Thomson NR, James KD, Harris DE, Quail MA, Kieser H, Harper D, Bateman A, Brown S, Chandra G, Chen CW, Collins M, Cronin A, Fraser A, Goble A, Hidalgo J, Hornsby T, Howarth S, Huang C-HC-H, Kieser T, Larke L, Murphy L, Oliver K, O'Neil S, Rabbinowitsch E, Rajandream MM-A, Rutherford K, Rutter S, Seeger K, Saunders D, Sharp S, Squares R, Squares S, Taylor K, Warren T, Wietzorrek A, Woodward J, Barrell BG, Parkhill J, Hopwood DA. 2002.

bioRxiv preprint doi: https://doi.org/10.1101/796722; this version posted March 26, 2020. The copyright holder for this preprint (which was not certified by peer review) is the author/funder, who has granted bioRxiv a license to display the preprint in perpetuity. It is made available under aCC-BY 4.0 International license.

Complete genome sequence of the model actinomycete Streptomyces coelicolor A3(2). Nature 417:141–147.

11. Gomez-Escribano JP, Song L, Fox DJ, Yeo V, Bibb MJ, Challis GL. 2012. Structure and biosynthesis of the unusual polyketide alkaloid coelimycin P1, a metabolic product of the cpk gene cluster of Streptomyces coelicolor M145. Chem Sci 3:2716–2720.

12. Castro JF, Razmilic V, Gomez-Escribano JP, Andrews B, Asenjo JA, Bibb MJ. 2015. Identification and Heterologous Expression of the Chaxamycin Biosynthesis Gene Cluster from Streptomyces leeuwenhoekii. Appl Environ Microbiol 81:5820–5831.

13. Gomez-Escribano JP, Bibb MJ. 2011. Engineering Streptomyces coelicolor for heterologous expression of secondary metabolite gene clusters. Microbial Biotechnology 4:207–215.

14. Gomez-Escribano JP, Bibb MJ. 2014. Heterologous expression of natural product biosynthetic gene clusters in Streptomyces coelicolor: from genome mining to manipulation of biosynthetic pathways. Journal of Industrial Microbiology & Biotechnology 41:425–431.

15. Kumelj T, Sulheim S, Wentzel A, Almaas E. 2018. Predicting Strain Engineering Strategies Using iKS1317: A Genome-Scale Metabolic Model of Streptomyces coelicolor. Biotechnology Journal 0:1800180.

16. Thanapipatsiri A, Claesen J, Gomez-Escribano J-P, Bibb M, Thamchaipenet A. 2015. A Streptomyces coelicolor host for the heterologous expression of Type III polyketide synthase genes. Microb Cell Fact 14.

bioRxiv preprint doi: https://doi.org/10.1101/796722; this version posted March 26, 2020. The copyright holder for this preprint (which was not certified by peer review) is the author/funder, who has granted bioRxiv a license to display the preprint in perpetuity. It is made available under aCC-BY 4.0 International license.

17. Yin J, Hoffmann M, Bian X, Tu Q, Yan F, Xia L, Ding X, Francis Stewart A, Müller R, Fu J, Zhang Y. 2015. Direct cloning and heterologous expression of the salinomycin biosynthetic gene cluster from Streptomyces albus DSM41398 in Streptomyces coelicolor A3(2). Scientific Reports 5:15081.

18. Nepal KK, Wang G. 2019. Streptomycetes: Surrogate hosts for the genetic manipulation of biosynthetic gene clusters and production of natural products. Biotechnology Advances 37:1–20.

19. Rutledge PJ, Challis GL. 2015. Discovery of microbial natural products by activation of silent biosynthetic gene clusters. Nature Reviews Microbiology 13:509–523.

20. Wentzel A, Bruheim P, Øverby A, Jakobsen ØM, Sletta H, Omara WAM, Hodgson DA, Ellingsen TE, Hopwood D, Bentley S, Chater K, Cerdeno-Tarraga A, Challis G, Thomson N, James K, Harris D, Quail M, Kieser H, Harper D, Klieneberger-Nobel E, Chater K, Hopwood D, Chater K, Bibb M, Lakey J, Lea E, Rudd B, Wright H, Hopwood D, Wright L, Hopwood D, Feitelson J, Hopwood D, Bibb M, Rokem J, Lantz S, Eliasson A, Nielsen J, Song S, Jeong Y, Kim P, Chun G, Rosa J, Neto AB, Hokka C, Badino A, Kieser T, Bibb M, Buttner M, Chater K, Hopwood D, Hayes A, Hobbs G, Smith C, Oliver S, Butler P, Evans C, Herbet D, Tempest D, Takano E, Gramajo H, Strauch E, Andres N, White J, Bibb M, Bruheim P, Sletta H, Bibb M, White J, Levine D, Hodgson D, Nieselt K, Battke F, Herbig A, Bruheim P, Wentzel A, Jakobsen O, Sletta H, Alam M, Merlo M, Moore J, Alam M, Merlo M, Hodgson D, Wellington E, Takano E, Breitling R, Battke F, Symons S, Nieselt K, Battke F, Herbig A, Wentzel A, Jakobsen O, Bonin M, Hodgson D, Wohlleben W, Ellingsen T, Nieselt K, Thomas L, Hodgson D, Wentzel A, Nieselt K, Ellingsen T, Moore J, Morrissey E, Legaie R, Wohlleben W, Rodriguez-Garcia A, Wentzel A, Sletta H, Consortium S,

bioRxiv preprint doi: https://doi.org/10.1101/796722; this version posted March 26, 2020. The copyright holder for this preprint (which was not certified by peer review) is the author/funder, who has granted bioRxiv a license to display the preprint in perpetuity. It is made available under aCC-BY 4.0 International license.

Ellingsen T, Bruheim P, Waldvogel E, Herbig A, Battke F, Amin R, Nentwich M, Nieselt K, Ellingsen T, Wentzel A, Hodgson D, Wohlleben W, Mast Y, Claessen D, Rink R, Jong W de, Siebring J, Vreugd P de, Boersma F, Dijkhuizen L, Wosten H, Bystrykh L, Fernandez-Moreno M, Herrema J, Malpartida F, Hopwood D, Dijkhuizen L, Villas-Boas S, Delicado D, Akesson M, Nielsen J, Christensen B, Nielsen J, Strauch E, Takano E, Baylis H, Bibb M, Martin J, Martin J, Demain A, Coisne S, Béchet M, Blondeau R, Gesheva V, Ivanova V, Gesheva R, Nakamura T, Yoshimoto A, Rollins M, Jensen S, Westlake D, Gorst-Allman C, Rudd B, Chang C-J, Floss H, Wasserman H, Shaw C, Sykes R, Cushley R, Bruheim P, Butler M, Ellingsen T, Jonsbu E, Christensen B, Nielsen J, Gunnarsson N, Bruheim P, Nielsen J, Rodriguez-Garcia A, Sola-Landa A, Apel K, Santos-Beneit F, Martin J, Santos-Beneit F, Rodriguez-Garcia A, Sola-Landa A, Martin J, Lambert R, Stratford M, Surowitz K, Pfister R. 2012. Optimized submerged batch fermentation strategy for systems scale studies of metabolic switching in Streptomyces coelicolor A3(2). BMC Systems Biology 6:59.

21. Wentzel A, Sletta H, Consortium S, Ellingsen TE, Bruheim P. 2012. Intracellular Metabolite Pool Changes in Response to Nutrient Depletion Induced Metabolic Switching in Streptomyces coelicolor. Metabolites 2:178–194.

22. Hu H, Zhang Q, Ochi K. 2002. Activation of Antibiotic Biosynthesis by Specified Mutations in the rpoB Gene (Encoding the RNA Polymerase β Subunit) of Streptomyces lividans. Journal of Bacteriology 184:3984–3991.

23. Braesel J, Tran TA, Eustáquio AS. 2019. Heterologous expression of the diazaquinomycin biosynthetic gene cluster. J Ind Microbiol Biotechnol.

bioRxiv preprint doi: https://doi.org/10.1101/796722; this version posted March 26, 2020. The copyright holder for this preprint (which was not certified by peer review) is the author/funder, who has granted bioRxiv a license to display the preprint in perpetuity. It is made available under aCC-BY 4.0 International license.

24. Kepplinger B, Morton-Laing S, Seistrup KH, Marrs ECL, Hopkins AP, Perry JD, Strahl H, Hall MJ, Errington J, Allenby NEE. 2018. Mode of Action and Heterologous Expression of the Natural Product Antibiotic Vancoresmycin. ACS Chem Biol 13:207–214.

25. Li T, Du Y, Cui Q, Zhang J, Zhu W, Hong K, Li W. 2013. Cloning, Characterization and Heterologous Expression of the Indolocarbazole Biosynthetic Gene Cluster from Marine-Derived Streptomyces sanyensis FMA. Marine Drugs 11:466–488.

26. Battke F, Symons S, Nieselt K. 2010. Mayday--integrative analytics for expression data. BMC Bioinformatics 11:121.

27. Jäger G, Battke F, Nieselt K. 2011. TIALA — Time series alignment analysis, p. 55–61. *In* 2011 IEEE Symposium on Biological Data Visualization (BioVis).

28. Liao Y, Smyth GK, Shi W. 2014. featureCounts: an efficient general purpose program for assigning sequence reads to genomic features. Bioinformatics 30:923–930.

29. Love MI, Huber W, Anders S. 2014. Moderated estimation of fold change and dispersion for RNA-seq data with DESeq2. Genome Biol 15:550.

30. Mi H, Muruganujan A, Ebert D, Huang X, Thomas PD. 2019. PANTHER version 14: more genomes, a new PANTHER GO-slim and improvements in enrichment analysis tools. Nucleic Acids Res 47:D419–D426.

31. Sánchez BJ, Zhang C, Nilsson A, Lahtvee P-J, Kerkhoven EJ, Nielsen J. 2017. Improving the phenotype predictions of a yeast genome-scale metabolic model by incorporating enzymatic constraints. Molecular Systems Biology 13:935.

bioRxiv preprint doi: https://doi.org/10.1101/796722; this version posted March 26, 2020. The copyright holder for this preprint (which was not certified by peer review) is the author/funder, who has granted bioRxiv a license to display the preprint in perpetuity. It is made available under aCC-BY 4.0 International license.

32. Robinson JL, Nielsen J. 2016. Integrative analysis of human omics data using biomolecular networks. Mol Biosyst 12:2953–2964.

33. Borodina I, Krabben P, Nielsen J. 2005. Genome-scale analysis of Streptomyces coelicolor A3(2) metabolism. Genome research 15:820–9.

34. Alam MT, Merlo ME, (stream) TSC, Hodgson DA, Wellington EM, Takano E, Breitling R. 2010. Metabolic modeling and analysis of the metabolic switch in Streptomyces coelicolor. BMC Genomics 11:202.

35. Amara A, Takano E, Breitling R. 2018. Development and validation of an updated computational model of Streptomyces coelicolor primary and secondary metabolism. BMC Genomics 19:519.

36. Kim MW, Sang Yi J, Kim J-NJJ-NNJ, Kim J-NJJ-NNJ, Kim MW, Kim B-GG. 2014. Reconstruction of a high-quality metabolic model enables the identification of gene overexpression targets for enhanced antibiotic production in streptomyces coelicolor A3(2). Biotechnology Journal 9:1185–1194.

37. Wang H, Marcišauskas S, Sánchez BJ, Domenzain I, Hermansson D, Agren R, Nielsen J, Kerkhoven EJ. 2018. RAVEN 2.0: A versatile toolbox for metabolic network reconstruction and a case study on Streptomyces coelicolor. PLOS Computational Biology 14:e1006541.

38. Mohite OS, Weber T, Kim HU, Lee SY. 2019. Genome-Scale Metabolic Reconstruction of Actinomycetes for Antibiotics Production. Biotechnology Journal 14:1800377.

bioRxiv preprint doi: https://doi.org/10.1101/796722; this version posted March 26, 2020. The copyright holder for this preprint (which was not certified by peer review) is the author/funder, who has granted bioRxiv a license to display the preprint in perpetuity. It is made available under aCC-BY 4.0 International license.

39. Toro L, Pinilla L, Avignone-Rossa C, Ríos-Estepa R. 2018. An enhanced genome-scale metabolic reconstruction of Streptomyces clavuligerus identifies novel strain improvement strategies. Bioprocess Biosyst Eng 41:657–669.

40. Licona-Cassani C, Marcellin E, Quek L-E, Jacob S, Nielsen LK. 2012. Reconstruction of the Saccharopolyspora erythraea genome-scale model and its use for enhancing erythromycin production. Antonie van Leeuwenhoek 102:493–502.

41. Valverde JR, Gullón S, Mellado RP. 2018. Modelling the metabolism of protein secretion through the Tat route in Streptomyces lividans. BMC Microbiology 18:59.

42. Lieven C, Beber ME, Olivier BG, Bergmann FT, Ataman M, Babaei P, Bartell JA, Blank LM, Chauhan S, Correia K, Diener C, Dräger A, Ebert BE, Edirisinghe JN, Faria JP, Feist A, Fengos G, Fleming RMT, Garcia-Jimenez B, Hatzimanikatis V, Helvoirt W van, Henry C, Hermjakob H, Herrgard MJ, Kim HU, King Z, Koehorst JJ, Klamt S, Klipp E, Lakshmanan M, Novere NL, Lee D-Y, Lee SY, Lee S, Lewis NE, Ma H, Machado D, Mahadevan R, Maia P, Mardinoglu A, Medlock GL, Monk J, Nielsen J, Nielsen LK, Nogales J, Nookaew I, Resendis O, Palsson B, Papin JA, Patil KR, Poolman M, Price ND, Richelle A, Rocha I, Sanchez B, Schaap P, Sheriff RSM, Shoaie S, Sonnenschein N, Teusink B, Vilaca P, Vik JO, Wodke JA, Xavier JC, Yuan Q, Zakhartsev M, Zhang C. 2018. Memote: A community-driven effort towards a standardized genome-scale metabolic model test suite. bioRxiv 350991.

43. Thiele I, Swainston N, Fleming RMT, Hoppe A, Sahoo S, Aurich MK, Haraldsdottir H, Mo ML, Rolfsson O, Stobbe MD, Thorleifsson SG, Agren R, Bölling C, Bordel S, Chavali AK, Dobson P, Dunn WB, Endler L, Hala D, Hucka M, Hull D, Jameson D, Jamshidi N, Jonsson

bioRxiv preprint doi: https://doi.org/10.1101/796722; this version posted March 26, 2020. The copyright holder for this preprint (which was not certified by peer review) is the author/funder, who has granted bioRxiv a license to display the preprint in perpetuity. It is made available under aCC-BY 4.0 International license.

JJ, Juty N, Keating S, Nookaew I, Le Novère N, Malys N, Mazein A, Papin JA, Price ND, Selkov E, Sigurdsson MI, Simeonidis E, Sonnenschein N, Smallbone K, Sorokin A, van Beek JHGM, Weichart D, Goryanin I, Nielsen J, Westerhoff HV, Kell DB, Mendes P, Palsson BØ. 2013. A community-driven global reconstruction of human metabolism. Nat Biotechnol 31.

44. Aung HW, Henry SA, Walker LP. 2013. Revising the Representation of Fatty Acid, Glycerolipid, and Glycerophospholipid Metabolism in the Consensus Model of Yeast Metabolism. Industrial Biotechnology 9:215–228.

45. Dobson PD, Smallbone K, Jameson D, Simeonidis E, Lanthaler K, Pir P, Lu C, Swainston N, Dunn WB, Fisher P, Hull D, Brown M, Oshota O, Stanford NJ, Kell DB, King RD, Oliver SG, Stevens RD, Mendes P. 2010. Further developments towards a genome-scale metabolic model of yeast. BMC Syst Biol 4:145.

46. Heavner BD, Smallbone K, Barker B, Mendes P, Walker LP. 2012. Yeast 5 – an expanded reconstruction of the Saccharomyces cerevisiae metabolic network. BMC Systems Biology 6:55.

47. Heavner BD, Smallbone K, Price ND, Walker LP. 2013. Version 6 of the consensus yeast metabolic network refines biochemical coverage and improves model performance. Database (Oxford) 2013:bat059.

48. Herrgård MJ, Swainston N, Dobson P, Dunn WB, Arga KY, Arvas M, Blüthgen N, Borger S, Costenoble R, Heinemann M, Hucka M, Le Novère N, Li P, Liebermeister W, Mo ML, Oliveira AP, Petranovic D, Pettifer S, Simeonidis E, Smallbone K, Spasić I, Weichart D, Brent R, Broomhead DS, Westerhoff HV, Kırdar B, Penttilä M, Klipp E, Palsson BØ, Sauer

bioRxiv preprint doi: https://doi.org/10.1101/796722; this version posted March 26, 2020. The copyright holder for this preprint (which was not certified by peer review) is the author/funder, who has granted bioRxiv a license to display the preprint in perpetuity. It is made available under aCC-BY 4.0 International license.

U, Oliver SG, Mendes P, Nielsen J, Kell DB. 2008. A consensus yeast metabolic network reconstruction obtained from a community approach to systems biology. Nat Biotechnol 26:1155–1160.

49. Lu H, Li F, Sánchez BJ, Zhu Z, Li G, Domenzain I, Marcišauskas S, Anton PM, Lappa D, Lieven C, Beber ME, Sonnenschein N, Kerkhoven EJ, Nielsen J. 2019. A consensus S. cerevisiae metabolic model Yeast8 and its ecosystem for comprehensively probing cellular metabolism. Nat Commun 10:1–13.

50. Hefzi H, Ang KS, Hanscho M, Bordbar A, Ruckerbauer D, Lakshmanan M, Orellana CA, Baycin-Hizal D, Huang Y, Ley D, Martinez VS, Kyriakopoulos S, Jiménez NE, Zielinski DC, Quek L-E, Wulff T, Arnsdorf J, Li S, Lee JS, Paglia G, Loira N, Spahn PN, Pedersen LE, Gutierrez JM, King ZA, Lund AM, Nagarajan H, Thomas A, Abdel-Haleem AM, Zanghellini J, Kildegaard HF, Voldborg BG, Gerdtzen ZP, Betenbaugh MJ, Palsson BO, Andersen MR, Nielsen LK, Borth N, Lee D-Y, Lewis NE. 2016. A Consensus Genome-scale Reconstruction of Chinese Hamster Ovary Cell Metabolism. Cell Systems 3:434-443.e8.

51. Kanehisa M. 2000. KEGG: Kyoto Encyclopedia of Genes and Genomes. Nucleic Acids Research 28:27–30.

52. Kanehisa M, Sato Y, Furumichi M, Morishima K, Tanabe M. 2019. New approach for understanding genome variations in KEGG. Nucleic Acids Research 47:D590–D595.

53. Karp PD, Billington R, Caspi R, Fulcher CA, Latendresse M, Kothari A, Keseler IM, Krummenacker M, Midford PE, Ong Q, Ong WK, Paley SM, Subhraveti P. 2017. The BioCyc collection of microbial genomes and metabolic pathways. Brief Bioinform.

bioRxiv preprint doi: https://doi.org/10.1101/796722; this version posted March 26, 2020. The copyright holder for this preprint (which was not certified by peer review) is the author/funder, who has granted bioRxiv a license to display the preprint in perpetuity. It is made available under aCC-BY 4.0 International license.

54. Hastings J, Owen G, Dekker A, Ennis M, Kale N, Muthukrishnan V, Turner S, Swainston N, Mendes P, Steinbeck C. 2016. ChEBI in 2016: Improved services and an expanding collection of metabolites. Nucleic Acids Res 44:D1214–D1219.

55. Moretti S, Martin O, Van Du Tran T, Bridge A, Morgat A, Pagni M. 2016. MetaNetX/MNXref – reconciliation of metabolites and biochemical reactions to bring together genome-scale metabolic networks. Nucleic Acids Res 44:D523–D526.

56. King ZA, Lu J, Dräger A, Miller P, Federowicz S, Lerman JA, Ebrahim A, Palsson BO, Lewis NE, J. H. 2016. BiGG Models: A platform for integrating, standardizing and sharing genome-scale models. Nucleic Acids Research 44:D515–D522.

57. The UniProt Consortium. 2019. UniProt: a worldwide hub of protein knowledge. Nucleic Acids Res 47:D506–D515.

58. Thiele I, Palsson BØ. 2010. A protocol for generating a high-quality genome-scale metabolic reconstruction. Nature protocols 5:93–121.

59. Flamholz A, Noor E, Bar-Even A, Milo R. 2012. eQuilibrator—the biochemical thermodynamics calculator. Nucleic Acids Res 40:D770–D775.

60. Chakrabarty AM. 1998. Nucleoside diphosphate kinase: role in bacterial growth, virulence, cell signalling and polysaccharide synthesis. Molecular Microbiology 28:875–882.

61. Yoshida M, Muneyuki E, Hisabori T. 2001. ATP synthase — a marvellous rotary engine of the cell. Nat Rev Mol Cell Biol 2:669–677.

bioRxiv preprint doi: https://doi.org/10.1101/796722; this version posted March 26, 2020. The copyright holder for this preprint (which was not certified by peer review) is the author/funder, who has granted bioRxiv a license to display the preprint in perpetuity. It is made available under aCC-BY 4.0 International license.

62. Getsin I, Nalbandian GH, Yee DC, Vastermark A, Paparoditis PC, Reddy VS, Saier MH. 2013. Comparative genomics of transport proteins in developmental bacteria: Myxococcus xanthus and Streptomyces coelicolor. BMC Microbiol 13:279.

63. Smirnov A, Esnault C, Prigent M, Holland IB, Virolle M-J. 2015. Phosphate Homeostasis in Conditions of Phosphate Proficiency and Limitation in the Wild Type and the phoP Mutant of Streptomyces lividans. PLoS One 10.

64. Orth JD, Thiele I, Palsson BØO. 2010. What is flux balance analysis? Nat Biotech 28:245–248.

65. Bordel S, Agren R, Nielsen J. 2010. Sampling the Solution Space in Genome-Scale Metabolic Networks Reveals Transcriptional Regulation in Key Enzymes. PLOS Computational Biology 6:e1000859.

66. Martín JF, Santos-Beneit F, Rodríguez-García A, Sola-Landa A, Smith MCM, Ellingsen TE, Nieselt K, Burroughs NJ, Wellington EMH. 2012. Transcriptomic studies of phosphate control of primary and secondary metabolism in Streptomyces coelicolor. Appl Microbiol Biotechnol 95:61–75.

67. Martín-Martín S, Rodríguez-García A, Santos-Beneit F, Franco-Domínguez E, Sola-Landa A, Martín JF. 2018. Self-control of the PHO regulon: the PhoP-dependent protein PhoU controls negatively expression of genes of PHO regulon in *Streptomyces coelicolor*. The Journal of Antibiotics 71:113–122.

bioRxiv preprint doi: https://doi.org/10.1101/796722; this version posted March 26, 2020. The copyright holder for this preprint (which was not certified by peer review) is the author/funder, who has granted bioRxiv a license to display the preprint in perpetuity. It is made available under aCC-BY 4.0 International license.

68. Sola-Landa A, Moura RS, Martín JF. 2003. The two-component PhoR-PhoP system controls both primary metabolism and secondary metabolite biosynthesis in Streptomyces lividans. Proc Natl Acad Sci U S A 100:6133–6138.

69. Martín JF, Rodríguez-García A, Liras P. 2017. The master regulator PhoP coordinates phosphate and nitrogen metabolism, respiration, cell differentiation and antibiotic biosynthesis: comparison in *Streptomyces coelicolor* and *Streptomyces avermitilis*. The Journal of Antibiotics 70:534–541.

70. Li L, Jiang W, Lu Y. 2017. A Novel Two-Component System, GluR-GluK, Involved in Glutamate Sensing and Uptake in Streptomyces coelicolor. Journal of Bacteriology 199.

71. Fink D, Weißschuh N, Reuther J, Wohlleben W, Engels A. 2002. Two transcriptional regulators GlnR and GlnRII are involved in regulation of nitrogen metabolism in *Streptomyces coelicolor* A3(2). Molecular Microbiology 46:331–347.

72. Martín JF. 2004. Phosphate Control of the Biosynthesis of Antibiotics and Other Secondary Metabolites Is Mediated by the PhoR-PhoP System: an Unfinished Story. Journal of Bacteriology 186:5197–5201.

73. Stirrett K, Denoya C, Westpheling J. 2009. Branched-chain amino acid catabolism provides precursors for the Type II polyketide antibiotic, actinorhodin, via pathways that are nutrient dependent. J Ind Microbiol Biotechnol 36:129–137.

74. Esnault C, Dulermo T, Smirnov A, Askora A, David M, Deniset-Besseau A, Holland I-B, Virolle M-J. 2017. Strong antibiotic production is correlated with highly active oxidative metabolism in Streptomyces coelicolor M145. Scientific Reports 7:200.

bioRxiv preprint doi: https://doi.org/10.1101/796722; this version posted March 26, 2020. The copyright holder for this preprint (which was not certified by peer review) is the author/funder, who has granted bioRxiv a license to display the preprint in perpetuity. It is made available under aCC-BY 4.0 International license.

75. Borodina I, Siebring J, Zhang J, Smith CP, Keulen G van, Dijkhuizen L, Nielsen J. 2008. Antibiotic Overproduction in Streptomyces coelicolor A3(2) Mediated by Phosphofructokinase Deletion. J Biol Chem 283:25186–25199.

76. Jonsbu E, Christensen B, Nielsen J. 2001. Changes of in vivo fluxes through central metabolic pathways during the production of nystatin by Streptomyces noursei in batch culture. Appl Microbiol Biotechnol 56:93–100.

77. Gallo G, Renzone G, Alduina R, Stegmann E, Weber T, Lantz AE, Thykaer J, Sangiorgi F, Scaloni A, Puglia AM. 2010. Differential proteomic analysis reveals novel links between primary metabolism and antibiotic production in Amycolatopsis balhimycina. PROTEOMICS 10:1336–1358.

78. Coze F, Gilard F, Tcherkez G, Virolle M-J, Guyonvarch A. 2013. Carbon-Flux Distribution within Streptomyces coelicolor Metabolism: A Comparison between the Actinorhodin-Producing Strain M145 and Its Non-Producing Derivative M1146. PLOS ONE 8:e84151.

79. Millan-Oropeza A, Henry C, Blein-Nicolas M, Aubert-Frambourg A, Moussa F, Bleton J, Virolle M-J. 2017. Quantitative Proteomics Analysis Confirmed Oxidative Metabolism Predominates in Streptomyces coelicolor versus Glycolytic Metabolism in Streptomyces lividans. J Proteome Res 16:2597–2613.

80. Ashburner M, Ball CA, Blake JA, Botstein D, Butler H, Cherry JM, Davis AP, Dolinski K, Dwight SS, Eppig JT, Harris MA, Hill DP, Issel-Tarver L, Kasarskis A, Lewis S, Matese JC, Richardson JE, Ringwald M, Rubin GM, Sherlock G. 2000. Gene ontology: tool for the unification of biology. The Gene Ontology Consortium. Nat Genet 25:25–29.

bioRxiv preprint doi: https://doi.org/10.1101/796722; this version posted March 26, 2020. The copyright holder for this preprint (which was not certified by peer review) is the author/funder, who has granted bioRxiv a license to display the preprint in perpetuity. It is made available under aCC-BY 4.0 International license.

81. The Gene Ontology Consortium. 2019. The Gene Ontology Resource: 20 years and still GOing strong. Nucleic Acids Res 47:D330–D338.

82. Stahl W, Sies H. 2003. Antioxidant activity of carotenoids. Molecular Aspects of Medicine 24:345–351.

83. Latifi A, Ruiz M, Zhang C-C. 2009. Oxidative stress in cyanobacteria. FEMS Microbiol Rev 33:258–278.

84. Zangar RC, Davydov DR, Verma S. 2004. Mechanisms that regulate production of reactive oxygen species by cytochrome P450. Toxicology and Applied Pharmacology 199:316–331.

85. Lamb DC, Ikeda H, Nelson DR, Ishikawa J, Skaug T, Jackson C, Omura S, Waterman MR, Kelly SL. 2003. Cytochrome P450 complement (CYPome) of the avermectin-producer Streptomyces avermitilis and comparison to that of Streptomyces coelicolor A3(2). Biochemical and Biophysical Research Communications 307:610–619.

86. Bednarz B, Kotowska M, Pawlik KJ. 2019. Multi-level regulation of coelimycin synthesis in Streptomyces coelicolor A3(2). Appl Microbiol Biotechnol 103:6423–6434.

87. Li X, Wang J, Li S, Ji J, Wang W, Yang K. 2015. ScbR- and ScbR2-mediated signal transduction networks coordinate complex physiological responses in *Streptomyces coelicolor*. Scientific Reports 5:14831.

88. Lee P-C, Umeyama T, Horinouchi S. 2002. afsS is a target of AfsR, a transcriptional factor with ATPase activity that globally controls secondary metabolism in Streptomyces coelicolor A3(2). Molecular Microbiology 43:1413–1430.

bioRxiv preprint doi: https://doi.org/10.1101/796722; this version posted March 26, 2020. The copyright holder for this preprint (which was not certified by peer review) is the author/funder, who has granted bioRxiv a license to display the preprint in perpetuity. It is made available under aCC-BY 4.0 International license.

89. Horinouchi S. 2003. AfsR as an integrator of signals that are sensed by multiple serine/threonine kinases in Streptomyces coelicolor A3(2). J IND MICROBIOL BIOTECHNOL 30:462–467.

90. Naseer N, Shapiro JA, Chander M. 2014. RNA-Seq analysis reveals a six-gene SoxR regulon in Streptomyces coelicolor. PLoS ONE 9:e106181.

91. Dela Cruz R, Gao Y, Penumetcha S, Sheplock R, Weng K, Chander M. 2010. Expression of the Streptomyces coelicolor SoxR regulon is intimately linked with actinorhodin production. J Bacteriol 192:6428–6438.

92. Shin J-H, Singh AK, Cheon D-J, Roe J-H. 2011. Activation of the SoxR regulon in Streptomyces coelicolor by the extracellular form of the pigmented antibiotic actinorhodin. J Bacteriol 193:75–81.

93. Valton J, Mathevon C, Fontecave M, Nivière V, Ballou DP. 2008. Mechanism and regulation of the Two-component FMN-dependent monooxygenase ActVA-ActVB from Streptomyces coelicolor. J Biol Chem 283:10287–10296.

94. Burgos HL, O'Connor K, Sanchez-Vazquez P, Gourse RL. 2017. Roles of Transcriptional and Translational Control Mechanisms in Regulation of Ribosomal Protein Synthesis in Escherichia coli. J Bacteriol 199.

95. Hesketh A, Chen WJ, Ryding J, Chang S, Bibb M. 2007. The global role of ppGpp synthesis in morphological differentiation and antibiotic production in Streptomyces coelicolor A3(2). Genome Biol 8:R161.

bioRxiv preprint doi: https://doi.org/10.1101/796722; this version posted March 26, 2020. The copyright holder for this preprint (which was not certified by peer review) is the author/funder, who has granted bioRxiv a license to display the preprint in perpetuity. It is made available under aCC-BY 4.0 International license.

96. Srivatsan A, Wang JD. 2008. Control of bacterial transcription, translation and replication by (p)ppGpp. Current Opinion in Microbiology 11:100–105.

97. Gaal T, Bartlett MS, Ross W, Turnbough CL, Gourse RL. 1997. Transcription Regulation by Initiating NTP Concentration: rRNA Synthesis in Bacteria. Science 278:2092–2097.

98. Chemler JA, Buchholz TJ, Geders TW, Akey DL, Rath CM, Chlipala GE, Smith JL, Sherman DH. 2012. Biochemical and Structural Characterization of Germicidin Synthase: Analysis of a Type III Polyketide Synthase that Employs Acyl-ACP as a Starter Unit Donor. J Am Chem Soc 134:7359–7366.

99. Xu J, Tozawa Y, Lai C, Hayashi H, Ochi K. 2002. A rifampicin resistance mutation in the rpoB gene confers ppGpp-independent antibiotic production in Streptomyces coelicolor A3(2). Mol Gen Genomics 268:179–189.

100. Craney A, Ozimok C, Pimentel-Elardo SM, Capretta A, Nodwell JR. 2012. Chemical Perturbation of Secondary Metabolism Demonstrates Important Links to Primary Metabolism. Chemistry & Biology 19:1020–1027.

101. Courtot M, Juty N, Knüpfer C, Waltemath D, Zhukova A, Dräger A, Dumontier M, Finney A, Golebiewski M, Hastings J, Hoops S, Keating S, Kell DB, Kerrien S, Lawson J, Lister A, Lu J, Machne R, Mendes P, Pocock M, Rodriguez N, Villeger A, Wilkinson DJ, Wimalaratne S, Laibe C, Hucka M, Le Novère N. 2011. Controlled vocabularies and semantics in systems biology. Mol Syst Biol 7:543.

102. Noor E, Haraldsdóttir HS, Milo R, Fleming RMT. 2013. Consistent Estimation of Gibbs Energy Using Component Contributions. PLOS Computational Biology 9:e1003098.

bioRxiv preprint doi: https://doi.org/10.1101/796722; this version posted March 26, 2020. The copyright holder for this preprint (which was not certified by peer review) is the author/funder, who has granted bioRxiv a license to display the preprint in perpetuity. It is made available under aCC-BY 4.0 International license.

103. Bar-Even A, Flamholz A, Noor E, Milo R. 2012. Thermodynamic constraints shape the structure of carbon fixation pathways. Biochimica et Biophysica Acta (BBA) - Bioenergetics 1817:1646–1659.

104. Feist AM, Henry CS, Reed JL, Krummenacker M, Joyce AR, Karp PD, Broadbelt LJ, Hatzimanikatis V, Palsson BØ. 2007. A genome-scale metabolic reconstruction for Escherichia coli K-12 MG1655 that accounts for 1260 ORFs and thermodynamic information. Molecular Systems Biology 3:121.

105. Elbourne LDH, Tetu SG, Hassan KA, Paulsen IT. 2017. TransportDB 2.0: a database for exploring membrane transporters in sequenced genomes from all domains of life. Nucleic Acids Research 45:D320–D324.

106. Saier MH, Reddy VS, Tsu BV, Ahmed MS, Li C, Moreno-Hagelsieb G. 2016. The Transporter Classification Database (TCDB): recent advances. Nucleic Acids Res 44:D372–D379.

107. NCBI Resource Coordinators. 2017. Database Resources of the National Center for Biotechnology Information. Nucleic Acids Research 45:D12–D17.

108. Jeske L, Placzek S, Schomburg I, Chang A, Schomburg D. 2019. BRENDA in 2019: a European ELIXIR core data resource. Nucleic Acids Res 47:D542–D549.

109. Fritzemeier CJ, Hartleb D, Szappanos B, Papp B, Lercher MJ. 2017. Erroneous energy-generating cycles in published genome scale metabolic networks: Identification and removal. PLOS Computational Biology 13:e1005494.

bioRxiv preprint doi: https://doi.org/10.1101/796722; this version posted March 26, 2020. The copyright holder for this preprint (which was not certified by peer review) is the author/funder, who has granted bioRxiv a license to display the preprint in perpetuity. It is made available under aCC-BY 4.0 International license.

110. Noor E. 2018. Removing both Internal and Unrealistic Energy-Generating Cycles in Flux Balance Analysis. arXiv:180304999 [q-bio].

111. Haraldsdóttir HS, Cousins B, Thiele I, Fleming RMT, Vempala S. 2017. CHRR: coordinate hit-and-run with rounding for uniform sampling of constraint-based models. Bioinformatics 33:1741–1743.

112. Kaufman DE, Smith RL. 1998. Direction Choice for Accelerated Convergence in Hit-and-Run Sampling. Operations Research 46:84–95.

113. Megchelenbrink W, Huynen M, Marchiori E. 2014. optGpSampler: An Improved Tool for Uniformly Sampling the Solution-Space of Genome-Scale Metabolic Networks. PLOS ONE 9:e86587.

114. Kieser T, Bibb MJ, Buttner M, Chater K, Hopwood DA. 2000. Practical Streptomyces Genetics. John Innes Foundation, Norwich, UK.

115. Claessen D, Rink R, Jong W de, Siebring J, Vreugd P de, Boersma FGH, Dijkhuizen L, Wösten HAB. 2003. A novel class of secreted hydrophobic proteins is involved in aerial hyphae formation in Streptomyces coelicolor by forming amyloid-like fibrils. Genes Dev 17:1714–1726.

116. Bystrykh LV, Fernández-Moreno MA, Herrema JK, Malpartida F, Hopwood DA, Dijkhuizen L. 1996. Production of actinorhodin-related “blue pigments” by Streptomyces coelicolor A3(2). J Bacteriol 178:2238–2244.

117. Gubbens J, Janus M, Florea BI, Overkleeft HS, van Wezel GP. 2012. Identification of glucose kinase-dependent and -independent pathways for carbon control of primary

bioRxiv preprint doi: https://doi.org/10.1101/796722; this version posted March 26, 2020. The copyright holder for this preprint (which was not certified by peer review) is the author/funder, who has granted bioRxiv a license to display the preprint in perpetuity. It is made available under aCC-BY 4.0 International license.

metabolism, development and antibiotic production in *Streptomyces coelicolor* by quantitative proteomics. Molecular Microbiology 86:1490–1507.

118. Wessel D, Flügge UI. 1984. A method for the quantitative recovery of protein in dilute solution in the presence of detergents and lipids. Anal Biochem 138:141–143.

119. Rappsilber J, Mann M, Ishihama Y. 2007. Protocol for micro-purification, enrichment, pre-fractionation and storage of peptides for proteomics using StageTips. Nat Protoc 2:1896–1906.

120. Distler U, Kuharev J, Navarro P, Levin Y, Schild H, Tenzer S. 2014. Drift time-specific collision energies enable deep-coverage data-independent acquisition proteomics. Nat Methods 11:167–170.

121. Andrews S. 2016. FastQC: a quality control tool for high throughput sequence data.

122. Kim D, Langmead B, Salzberg SL. 2015. HISAT: a fast spliced aligner with low memory requirements. Nat Methods 12:357–360.

123. Li H, Handsaker B, Wysoker A, Fennell T, Ruan J, Homer N, Marth G, Abecasis G, Durbin R, 1000 Genome Project Data Processing Subgroup. 2009. The Sequence Alignment/Map format and SAMtools. Bioinformatics 25:2078–2079.

124. Okonechnikov K, Conesa A, García-Alcalde F. 2016. Qualimap 2: advanced multi-sample quality control for high-throughput sequencing data. Bioinformatics 32:292–294.

125. Battke F, Nieselt K. 2011. Mayday SeaSight: combined analysis of deep sequencing and microarray data. PLoS ONE 6:e16345.

bioRxiv preprint doi: https://doi.org/10.1101/796722; this version posted March 26, 2020. The copyright holder for this preprint (which was not certified by peer review) is the author/funder, who has granted bioRxiv a license to display the preprint in perpetuity. It is made available under aCC-BY 4.0 International license.

126. Huang DW, Sherman BT, Lempicki RA. 2009. Bioinformatics enrichment tools: paths toward the comprehensive functional analysis of large gene lists. Nucleic Acids Res 37:1–13.

127. Huang DW, Sherman BT, Lempicki RA. 2009. Systematic and integrative analysis of large gene lists using DAVID bioinformatics resources. Nat Protoc 4:44–57.

128. Szklarczyk D, Gable AL, Lyon D, Junge A, Wyder S, Huerta-Cepas J, Simonovic M, Doncheva NT, Morris JH, Bork P, Jensen LJ, Mering C von. 2019. STRING v11: protein-protein association networks with increased coverage, supporting functional discovery in genome-wide experimental datasets. Nucleic Acids Res 47:D607–D613.

129. Perez-Riverol Y, Csordas A, Bai J, Bernal-Llinares M, Hewapathirana S, Kundu DJ, Inuganti A, Griss J, Mayer G, Eisenacher M, Pérez E, Uszkoreit J, Pfeuffer J, Sachsenberg T, Yilmaz S, Tiwary S, Cox J, Audain E, Walzer M, Jarnuczak AF, Ternent T, Brazma A, Vizcaíno JA. 2019. The PRIDE database and related tools and resources in 2019: improving support for quantification data. Nucleic Acids Res 47:D442–D450.